

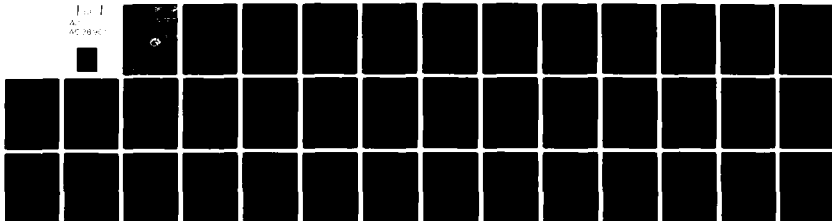
AD-A098 901

NAVAL OCEAN RESEARCH AND DEVELOPMENT ACTIVITY NSTL S--ETC F/G 20/4
AN ANALYSIS OF MODELLED SHEAR DISTRIBUTIONS DURING THE MILE EXP--ETC(U)
FEB 81 A C WARM-VARNAS, G DAWSON
NORDA-TN-84

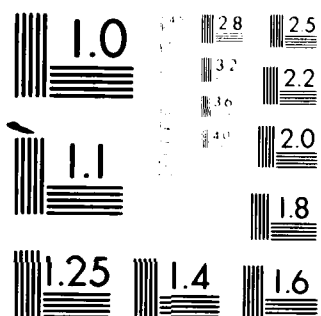
NL

UNCLASSIFIED

1
AC 20/4



END
DATE
FILMED
6 81
DTIC



MICROCOPY RESOLUTION TEST CHART
NATIONAL BUREAU OF STANDARDS-1963-A

LEVEL II

BS

(12)

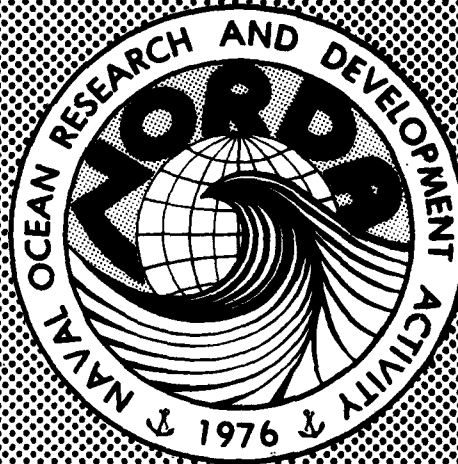
✓ NORDA Technical Note 84

Naval Ocean Research
and Development Activity
NSTL Station, Mississippi 39529

An Analysis of Modelled Shear Distribution During MILE

See 1473.

AD A098901



DTIC
ELECTE
MAY 14 1981
S E

DTIC FILE COPY

Unlimited Distribution

Alex C. Warn-Varnas
Gretchen Dawson

Numerical Modeling Division
Ocean Science and Technology Laboratory

FEBRUARY 1981

81 5 14 002

ABSTRACT

The shear in the mixed layer was forecasted and studied for the duration of the MILE experiment. The forecasting was done with the Warn-Varnas and Piacsek (1979) model.

The forecasts were initiated from data and driven by the experimentally-measured wind stress, radiation, and latent and sensible heat flux. The duration of forecasts spanned a time frame of several days to a month.

The problem of understanding the shear in the mixed-layer region during MILE was approached from two points of view. First, the basic dynamic processes that generate shear were considered. Second, statistical distributions of shear as a function of depth and time were computed.

The basic dynamics can be understood by decomposing the velocity into an Ekman-type component and an inertial component. The vertical structure of this velocity can be visualized as a superposition of an inertial oscillation onto an Ekman spiral; the inertial oscillations being excited by abrupt changes in wind stress. In most cases, the maximum shear occurred at the bottom of the mixed layer and near the surface. In some cases, two shear maxima regions were found below the surface. These cases involved situations of rising wind stress from a previous history of low magnitude.

In the statistical approach, scatter diagrams of shear versus Brunt-Vaisala frequency are computed. At different depths, these scatter diagrams show the relationship of mixing, as indicated by the Brunt-Vaisala frequency, to shear. The simulated magnitudes of shear are in the range of the experimental results of R. E. Davis, et al.

Probability diagrams of calculated flux Richardson numbers as a function of depth are also computed. These probability diagrams show a shift toward higher Richardson numbers as the depth increases. This reflects the fact that the penetration of turbulence and mixing tend to decrease, on the average, with depth.

CONTENTS

	PAGE
LIST OF ILLUSTRATIONS	iv
I. INTRODUCTION	1
II. EQUATIONS OF THE ONE-DIMENSIONAL WP MODEL	3
A. THE MEAN FIELD EQUATIONS	3
B. THE WP EQUATIONS FOR THE SECOND-ORDER CORRELATIONS	3
C. BOUNDARY CONDITIONS	4
D. DISSIPATION FUNCTION	4
III. RESULTS AND DISCUSSION	5
A. STATISTICAL DISTRIBUTIONS OF STRATIFICATION AND SHEAR	5
B. CASE OF CONSTANT WIND STRESS WITH NO HEAT FLUX	6
C. LOW AND HIGH WIND STRESS CASES DURING MILE	6
IV. CONCLUSION	7
V. ACKNOWLEDGEMENTS	8
VI. REFERENCES	8
APPENDIX: THE FINITE DIFFERENCE SCHEMES	33

Accession For	
NTIS GRA&I	<input checked="" type="checkbox"/>
DTIC TAB	<input type="checkbox"/>
Unannounced	<input type="checkbox"/>
Justification	

1. *SECRET*
 2. *CONFIDENTIAL*
 3. *CONFIDENTIAL*
 4. *CONFIDENTIAL*
 5. *CONFIDENTIAL*
 6. *CONFIDENTIAL*
 7. *CONFIDENTIAL*
 8. *CONFIDENTIAL*
 9. *CONFIDENTIAL*
 10. *CONFIDENTIAL*
 11. *CONFIDENTIAL*
 12. *CONFIDENTIAL*
 13. *CONFIDENTIAL*
 14. *CONFIDENTIAL*
 15. *CONFIDENTIAL*
 16. *CONFIDENTIAL*
 17. *CONFIDENTIAL*
 18. *CONFIDENTIAL*
 19. *CONFIDENTIAL*
 20. *CONFIDENTIAL*
 21. *CONFIDENTIAL*
 22. *CONFIDENTIAL*
 23. *CONFIDENTIAL*
 24. *CONFIDENTIAL*
 25. *CONFIDENTIAL*
 26. *CONFIDENTIAL*
 27. *CONFIDENTIAL*
 28. *CONFIDENTIAL*
 29. *CONFIDENTIAL*
 30. *CONFIDENTIAL*
 31. *CONFIDENTIAL*
 32. *CONFIDENTIAL*
 33. *CONFIDENTIAL*
 34. *CONFIDENTIAL*
 35. *CONFIDENTIAL*
 36. *CONFIDENTIAL*
 37. *CONFIDENTIAL*
 38. *CONFIDENTIAL*
 39. *CONFIDENTIAL*
 40. *CONFIDENTIAL*
 41. *CONFIDENTIAL*
 42. *CONFIDENTIAL*
 43. *CONFIDENTIAL*
 44. *CONFIDENTIAL*
 45. *CONFIDENTIAL*
 46. *CONFIDENTIAL*
 47. *CONFIDENTIAL*
 48. *CONFIDENTIAL*
 49. *CONFIDENTIAL*
 50. *CONFIDENTIAL*
 51. *CONFIDENTIAL*
 52. *CONFIDENTIAL*
 53. *CONFIDENTIAL*
 54. *CONFIDENTIAL*
 55. *CONFIDENTIAL*
 56. *CONFIDENTIAL*
 57. *CONFIDENTIAL*
 58. *CONFIDENTIAL*
 59. *CONFIDENTIAL*
 60. *CONFIDENTIAL*
 61. *CONFIDENTIAL*
 62. *CONFIDENTIAL*
 63. *CONFIDENTIAL*
 64. *CONFIDENTIAL*
 65. *CONFIDENTIAL*
 66. *CONFIDENTIAL*
 67. *CONFIDENTIAL*
 68. *CONFIDENTIAL*
 69. *CONFIDENTIAL*
 70. *CONFIDENTIAL*
 71. *CONFIDENTIAL*
 72. *CONFIDENTIAL*
 73. *CONFIDENTIAL*
 74. *CONFIDENTIAL*
 75. *CONFIDENTIAL*
 76. *CONFIDENTIAL*
 77. *CONFIDENTIAL*
 78. *CONFIDENTIAL*
 79. *CONFIDENTIAL*
 80. *CONFIDENTIAL*
 81. *CONFIDENTIAL*
 82. *CONFIDENTIAL*
 83. *CONFIDENTIAL*
 84. *CONFIDENTIAL*
 85. *CONFIDENTIAL*
 86. *CONFIDENTIAL*
 87. *CONFIDENTIAL*
 88. *CONFIDENTIAL*
 89. *CONFIDENTIAL*
 90. *CONFIDENTIAL*
 91. *CONFIDENTIAL*
 92. *CONFIDENTIAL*
 93. *CONFIDENTIAL*
 94. *CONFIDENTIAL*
 95. *CONFIDENTIAL*
 96. *CONFIDENTIAL*
 97. *CONFIDENTIAL*
 98. *CONFIDENTIAL*
 99. *CONFIDENTIAL*
 100. *CONFIDENTIAL*

LIST OF ILLUSTRATIONS

	PAGE
FIGURE 1: The Atmospheric Forcing Fluxes of MILE.	11
FIGURE 2: Distribution of Flux Richardson Numbers at 5 Meters.	12
FIGURE 3: Distribution of Flux Richardson Numbers at 10 Meters.	13
FIGURE 4: Distribution of Flux Richardson Numbers at 20 Meters.	14
FIGURE 5: Scatter Diagram of Shear Versus Stratification at 1-Meter Depth.	15
FIGURE 6: Scatter Diagram of Shear Versus Stratification at 20-Meter Depth.	16
FIGURE 7: Scatter Diagram of Shear Versus Stratification at 30-Meter Depth.	17
FIGURE 8: Total Horizontal Velocities Versus Depth.	18
FIGURE 9: Ekman Velocities Versus Depth.	19
FIGURE 10: Inertial Velocities Versus Depth.	20
FIGURE 11: Derivatives of Total Horizontal Velocities Versus Depth.	21
FIGURE 12: Velocity Hodographs at 1-Meter Depth.	22
FIGURE 13: Velocity Hodographs at 9-Meter Depth.	23
FIGURE 14: Total Velocities Versus Depth on Day 7.92.	24
FIGURE 15: Ekman Velocities Versus Depth on Day 7.92.	25
FIGURE 16: Shear Versus Depth on Day 7.92.	26
FIGURE 17: Inertial Velocities Versus Depth on Day 8.58.	27
FIGURE 18: Shear Versus Depth on Day 8.58.	28
FIGURE 19: Total Velocities Versus Depth on Day 18.58.	29
FIGURE 20: Shear Versus Depth on Day 18.58.	30
FIGURE 21: Velocity Hodographs for MILE from Day 2 to 7 at a Depth of 1 Meter.	31
FIGURE 22: Velocity Hodographs for MILE from Day 32 to 36 at a Depth of 30 Meters.	32

AN ANALYSIS OF MODELLED SHEAR DISTRIBUTIONS DURING THE MILE EXPERIMENT

I. INTRODUCTION

The propagation of internal waves in the ocean is strongly affected by gradients in density and current velocity. Such regions cause reflection, refraction, absorption, and breaking of the waves. Under certain conditions, the waves can also grow in regions of velocity shear. To be able to predict the propagation of a group of internal waves in the upper ocean, one must be able to predict in some deterministic/statistical sense the properties of this upper ocean environment; in particular, the spatial and temporal distribution of density and velocity gradients and regions of turbulence activity. Since temperature measurements are much easier to carry out than current measurements, and temperature data sets are in great abundance, emphasis will be on measurements and theoretical understanding of current shear in the coming year.

The present study deals with the problem of current shear in the mixed layer. The shear in the mixed layer was forecasted and studied for the duration of the MILE experiment. The forecasting was done with the Warn-Varnas and Piacsek (1979) model, referred hereafter as the WP model.

The WP model is a one-dimensional, higher-order closure model in the sense that it retains the triple-correlation terms. The model contains forecast equations for the mean fields, second-order correlations, and third-order correlations. The finite-difference solution of the equations is formulated without any critical Richardson number cut-off criteria of the turbulence, and, therefore, the effects of shear penetration of turbulence at the bottom of the mixed layer are preserved.

The forecasts were initiated from data and driven by the experimentally-measured wind stress, radiation, and latent and sensible heat flux. The duration of forecasts ranged from several days to a month.

The problem of understanding the shear in the mixed layer during MILE was approached from two points of view. First, the basic dynamic processes that generate shear were considered. Second, the statistical distributions of shear as a function of depth and time were calculated.

The basic dynamics can be understood by decomposing the velocity into an Ekman-type component and an inertial component. The Ekman components are obtained from a balance between the second-order correlation terms and the Coriolis terms.

The vertical structure of this velocity can be visualized as a superposition of an inertial oscillation onto an Ekman spiral, the inertial oscillations being excited by abrupt changes in wind stress.

This hypothesis was illustrated by turning on a constant wind stress, with no heat flux, for one of the MILE temperature profiles and performing a numerical simulation of several inertial periods. Throughout the mixed layer, the velocity hodographs showed circles of constant amplitudes versus depth. The center of the circles versus depth were displaced as if sitting on top of an Ekman spiral. The amplitude of this inertial velocity was constant throughout the mixed-layer depth and was zero below the mixed layer. The maximum shears occurred at the bottom of the mixed layer and near the surface. Both components of the velocity, the Ekman and inertial, showed appreciable shear at the bottom of the mixed layer.

Next, a time was selected during MILE when there was no wind stress. In this case, it was found that the Ekman part of the velocity was zero and the shear at the bottom of the mixed layer was due to the inertial component of the velocity only. In another case, a time was selected when the stress peaked around 4.5 dynes/cm², and a shear of 5×10^{-2} cm/sec was found at the bottom of the mixed layer. The magnitudes of the Ekman versus the inertial parts of the shear were 3×10^{-2} cm/sec and 4×10^{-6} cm/sec, respectively. Also considered was a case that involved a situation where the wind stress was rising from a previous history of low magnitude. The maximum shear occurred at the penetration depths of the turbulence generated by this rising wind stress. The next largest shear was located further down at the bottom of the mixed layer and was due to a previously-excited inertial wave.

In the statistical approach, scatter diagrams of shear versus Brunt-Vaisala frequency are computed. At different depths, these scatter diagrams show the relationship of mixing to shear as indicated by the Brunt-Vaisala frequency. The simulated magnitudes of shear are in the range of the experimental results of R. E. Davis, et al.

Probability diagrams of calculated Richardson numbers as a function of depth are also computed. These probability diagrams show a shift toward higher Richardson numbers as the depth increases. This reflects the fact that the penetration of turbulence and mixing tend to decrease, on the average, with depth.

II. EQUATIONS OF THE ONE-DIMENSIONAL WP MODEL

A. THE MEAN FIELD EQUATIONS

$$\frac{\partial \bar{u}}{\partial t} = - \frac{\partial}{\partial z} \overline{u'w'} + f\bar{v} + \nu \frac{\partial^2 \bar{u}}{\partial z^2}, \quad (2.1)$$

$$\frac{\partial \bar{v}}{\partial t} = - \frac{\partial}{\partial z} \overline{v'w'} - f\bar{u} + \nu \frac{\partial^2 \bar{v}}{\partial z^2}, \quad (2.2)$$

$$\frac{\partial \bar{T}}{\partial t} = - \frac{\partial}{\partial z} \overline{w'T'} + \kappa \frac{\partial^2 \bar{T}}{\partial z^2} + \frac{1}{\rho_0 c_p} \frac{\partial F}{\partial z}, \quad (2.3)$$

where ρ_0 is the mean density, F is the downward flux of solar radiation, and c_p is the specific heat at constant pressure.

B. THE WP EQUATIONS FOR THE SECOND-ORDER CORRELATIONS

$$\begin{aligned} \frac{\partial \overline{u'_i u'_j}}{\partial t} = & - \left(\overline{u'_i w'} \frac{\partial \bar{u}_j}{\partial z} + \overline{u'_j w'} \frac{\partial \bar{u}_i}{\partial z} \right) + \alpha g (\overline{u'_i T'} \delta_{3i} + \overline{u'_j T'} \delta_{3j}) \\ & - C_1 \left(\frac{\epsilon}{k} \right) \overline{u'_i u'_j} - 2kC_2 \left(\frac{\partial \bar{u}_i}{\partial x_j} + \frac{\partial \bar{u}_j}{\partial x_i} \right) + C_3 \epsilon \delta_{ij} - \frac{\partial}{\partial z} (\overline{u'_i u'_j w'}), \end{aligned} \quad (2.4)$$

$$\begin{aligned} \frac{\partial \overline{u'_i T'}}{\partial t} = & - \overline{u'_i w'} \frac{\partial \bar{T}}{\partial z} - \overline{w' T'} \frac{\partial \bar{u}_i}{\partial z} + \alpha g \overline{T' T'} \delta_{i3} \\ & - C_{it} \left(\frac{\epsilon}{k} \right) \overline{u'_i T'} - \frac{\partial}{\partial z} (\overline{u'_i w' T'}), \end{aligned} \quad (2.5)$$

$$\frac{\partial \overline{T' T'}}{\partial t} = - \overline{w' T'} \frac{\partial \bar{T}}{\partial z} - C_4 \left(\frac{\epsilon}{k} \right) \overline{T' T'} - \frac{\partial}{\partial z} (\overline{w' T' T'}), \quad (2.6)$$

where ϵ is the dissipation function.

The constants are set according to Mellor (1973); $C_1 = 3.19$, $C_2 = 0.056$, $C_3 = 1.47$, $C_{1t} = 4.78$, and $C_4 = 1.87$. They are based mostly on experimental measurements in the neutral, constant-flux layer and grid-generated, constant shear flow.

The equations for the triple correlations are given in the WP paper with the decay terms changed to the form $-2.48 \frac{E}{k}$ x triple correlations. The finite-difference scheme used to solve the equations is described in the Appendix.

C. BOUNDARY CONDITIONS

At the bottom boundary, all velocities are set to zero and the temperature is prescribed. At the top boundary, or surface, one uses

$$\begin{aligned}\overline{u'w'} &= -\tau_x \\ \overline{v'w'} &= -\tau_y \\ \overline{w'T'} &= -H\end{aligned}\tag{2.7}$$

where H is the sum of the latent, sensible, and back radiation fluxes, and τ_x and τ_y are the wind stresses along the x and y axis.

D. DISSIPATION FUNCTION

The dissipation function is defined as

$$\epsilon/k^2/\lambda\tag{2.8}$$

where $\lambda = .1886$ as obtained from Mellor (1973). For the WP model, ϵ is defined as

$$\epsilon = \frac{\beta z}{1 + \beta z/\lambda}\tag{2.9}$$

where $\beta = \frac{m_2 \int_0^\infty z k^{-1/2} dz}{\int_0^\infty k^{-1/2} dz}$, β is Von Karman's constant, and m_2 is an empirical constant.

III. RESULTS AND DISCUSSION

A. STATISTICAL DISTRIBUTIONS OF STRATIFICATIONS AND SHEAR

A numerical simulation of the MILE experiment with the WP one-dimensional model was performed. The data used was that of Miyake (1978). The driving fluxes that arose from this data are shown in figure 1. The model was initialized from measured temperature profiles at 10:00z August 2, 1977. Then, the measured wind stress, solar radiation, back radiation, and sensible and latent heat flux forced the model via the boundary conditions as given in Warn-Varnas et al. (1981). Probability distributions of flux Richardson numbers were calculated at various depths for the duration of MILE (about 30 days). The results are shown in figures 2 through 4. The flux Richardson number was defined as

$$R_F = \frac{-\alpha g \overline{w'T'}}{-\overline{u'w'} \frac{\partial \overline{u}}{\partial z} - \overline{v'w'} \frac{\partial \overline{v}}{\partial z}}, \quad (3.1)$$

and the observations were 4 hours apart. Near the surface, inversions in temperature can occur due to cooling. This results in negative values of the flux Richardson number. In general, the probability of finding the low-value Richardson numbers is greatest near the surface since the chances of turbulence existing there are the greatest. For turbulence to penetrate further into the mixed layer, larger wind stresses or cooling fluxes are required. These larger values of forcing fluxes are less probable, and, therefore, the values of the Richardson numbers increase with depth, indicating that there is less turbulence at greater depths. This fact is illustrated by the shift of the probability distribution diagrams toward higher Richardson numbers as the depth increases (figures 2 through 4).

An estimate of the distribution of stratification and shear during MILE can be obtained from scatter diagrams for various depths. These diagrams have been computed from the model results at intervals of 4 hours. The results are shown in figures 5 through 7. The units are cgs.

In general, the largest shears are around the bottom of the mixed layer, which is located around 30 meters most of the time (figure 7). The next largest shears are located around the surface (figure 5). The region which is the mixed layer most of the time shows smaller shears since the velocities there change less with depth (figure 6). The largest stratifications are near the bottom of the mixed layer where the thermocline is located (figure 7).

B. CASE OF CONSTANT WIND STRESS WITH NO HEAT FLUX

In order to illustrate the consequences of wind-generated shear turbulence on mixed-layer dynamics, a constant wind stress of $\tau_x = \tau_y = 2.5 \text{ dynes/cm}^2$ is prescribed, and the problem is initialized from the MILE temperature profile on day number 7. The results, about four inertial periods later, are shown in figures 8 through 13. The velocity can be decomposed into Ekman and inertial components as $\vec{v} = \vec{v}_E + \vec{v}_I$. It is assumed that the Ekman or shear-type components of the velocity are determined by the equations

$$\bar{u}_E = -\frac{1}{f} \frac{\partial \overline{v'w'}}{\partial z}, \quad (3.2)$$

$$\bar{v}_E = \frac{1}{f} \frac{\partial \overline{u'w'}}{\partial z}. \quad (3.3)$$

Nomitsu (1933) gives further details on an analytical analog of such a decomposition.

The largest shear is located near the bottom of the mixed layer (figure 11). There, the Ekman and inertial components of the velocity both contribute to the shear (figures 9 and 10). An interesting result is shown in figure 10; the amplitude of the inertial velocity is constant with depth and the mixed layer oscillates as a "slab".

Figures 12 and 13 show velocity hodographs at depths of 1 and 9 meters. Again, one can see a constant amplitude oscillation in the mixed layer. A qualitative picture of the dynamics can be constructed by visualizing an Ekman spiral oriented about 50 degrees to the right of the wind stress with a constant amplitude inertial oscillation superposed on it. Thus, as one goes down into the ocean, the hodographs shift to the right just as if they were following the Ekman spiral.

C. LOW AND HIGH WIND STRESS CASES DURING MILE

Around day number 8, the wind stress peaks at about 4 dynes/cm^2 and, then, around day 8.5 diminishes to zero (figure 1). The results for day number 8 are shown in figures 14 through 16. As in the previous example of constant wind stresses, the Ekman and inertial parts of the velocity solution contribute to the shear at the bottom of the mixed layer. The resultant shear magnitude is about 0.1 cm/sec (figure 16). On day number 8.58, both the wind stress and the Ekman part of the velocity solution tend toward zero. The total velocity is now equal to the inertial component of the velocity shown in figure 17. The resultant shear is shown in figure 18. Thus, even in a case when there is no wind stress and no

Ekman component of the velocity solution, there still is a shear present at the bottom of the mixed layer due to the inertial component of the velocity solutions. Once an inertial wave is excited, it will exist till it is damped out by the ambient ocean. An average damping time is about 10 days (Pollard, 1970). At this point, one might tend to think that model-simulated shear exists only at the top (surface) and bottom of mixed layers. This is not the case, as is shown in the next example.

On day number 18.58, the wind stress began increasing after a period when it was constant, and then began decreasing. The largest shear is now located around the penetration depth of the Ekman velocity, which is about 10 meters (figure 20). The next largest shear is past 30 meters and is caused by a previously-excited inertial wave.

The qualitative picture is one of an Ekman velocity being matched to a previously-excited inertial wave (figure 19). The picture can be pursued further by analyzing the excitations of inertial waves in time during MILE. Figures 21 through 22 show the MILE velocity hodographs at depths of 1 and 30 meters. The graphics do not have enough resolution in time, and, therefore, lines that should be arcs of a circle appear as straight lines. In figure 21, the time span from 2 to 7 days is covered and a range of inertial amplitudes, indicating that as wind stress magnitude varies the amplitudes of the excited inertial waves vary. In figure 22, the time span from 32 to 35 days at a depth of 30 meters is covered, and one can see that a constant amplitude inertial wave was present. This inertial wave was excited by a large storm from day 22 to day 25. Since, at that time, the temperature mixed layer was already pre-mixed to about 30 meters, the large wind stress that peaked at 5 dynes/cm^2 was able to excite a large amplitude inertial wave at a depth of 30 meters. Similarly, on day number 18.58, there was a large inertial wave present that had been excited during the wind storms from day 9 to day 14. This inertial wave penetrated to a depth of almost 30 meters (figure 19).

IV. CONCLUSION

The shear was forecasted for the MILE experiment with a one-dimensional higher-order closure mixed layer model by Warn-Varnas and Piacsek (1979). The statistical distributions of shear and stratification were analyzed in various ways. The probability distribution of flux Richardson numbers showed a shift

toward higher Richardson numbers as the depth of penetration into the ocean increased. This situation arises because the depth of penetration of shear-produced turbulence into the ocean depends upon the strength of the wind stress. The larger values of wind stress are less probable and, therefore, the probable values of the Richardson number increase with depth, indicating that, on the average, there is less turbulence with increased depth.

The distribution of shear and stratification during MILE were obtained by computing scatter diagrams at various depths. These scatter diagrams showed that, most of the time, the largest shears are located around the bottom of the mixed layer and near the surface. Within the mixed layer, the shears are usually smaller, indicating a high homogeneity of velocity profiles. For transient cases, there are exceptions, as will be pointed out later. The maximum shears were distributed in the range of 2×10^{-2} to 7×10^{-2} (cm/sec). These values are in the range of the experimental results of R. E. Davis, et al. (1980).

Steady and unsteady cases of high and low wind stress were analyzed. The analysis was performed by decomposing the velocity into an Ekman and inertial part. The Ekman or shear part was dependent upon the wind stress being present at the surface, while the inertial part was influenced by present and past wind stresses. Once an inertial wave was excited, it remained for about 10 days till it was damped out. The hodographs showed that as the wind stress amplitudes changed, the amplitudes of excited inertial waves also changed. The Ekman part of the velocity diminished to zero as the wind stress decreased to zero.

A transient case was found in which the maximum shear does not occur at the bottom of the temperature mixed-layer depth. This can happen when there is a building Ekman part of the velocity solution, generated by a rising wind stress, being superposed on a previously-excited inertial wave.

V. ACKNOWLEDGMENT

This work was sponsored by NORDA Code 500.

VI. REFERENCES

- Davis, R. E., deSzoek, R., Halpern, D., and Niiler, P., "Variability and Dynamics of the Upper Ocean During MILE," submitted to Journal of Physical Oceanography 1980.
- Mellor, G. L., "Analytic prediction of the properties of stratified planetary surface layers," J. Atmos. Sci., 30, 1061 (1973).

- Miyake, M., "Oceanographic observations at Ocean Station P," Pacific Marine Science Report 78-1, Institute of Ocean Sciences, Sidney, B. C. (1978).
- Nomitsu, T., "A theory of the rising stage of drift current in the ocean," Mem. Coll. Sci., Kyoto, 16, No. 2, (1933).
- Pollard, R. T., and Millard, R. C., "Comparison between observed and simulated wind-generated inertial oscillations," Deep-Sea Research 17, 813-821, (1970).
- Warn-Varnas, A. C., Dawson, G. D., and Martin, P. T., "Forecast and Studies in the Oceanic Mixed Layer During the MILE Experiment," Geophys. Astrophys. Fluid Dynamics. To appear in February issue 1981.
- Warn-Varnas, A. C. and Piacsek, S. A., "An investigation of the importance of third-order correlations and choice of length scale in mixed layer modelling," Geophys. Astrophys. Fluid Dynamics, 13, 225 (1979).

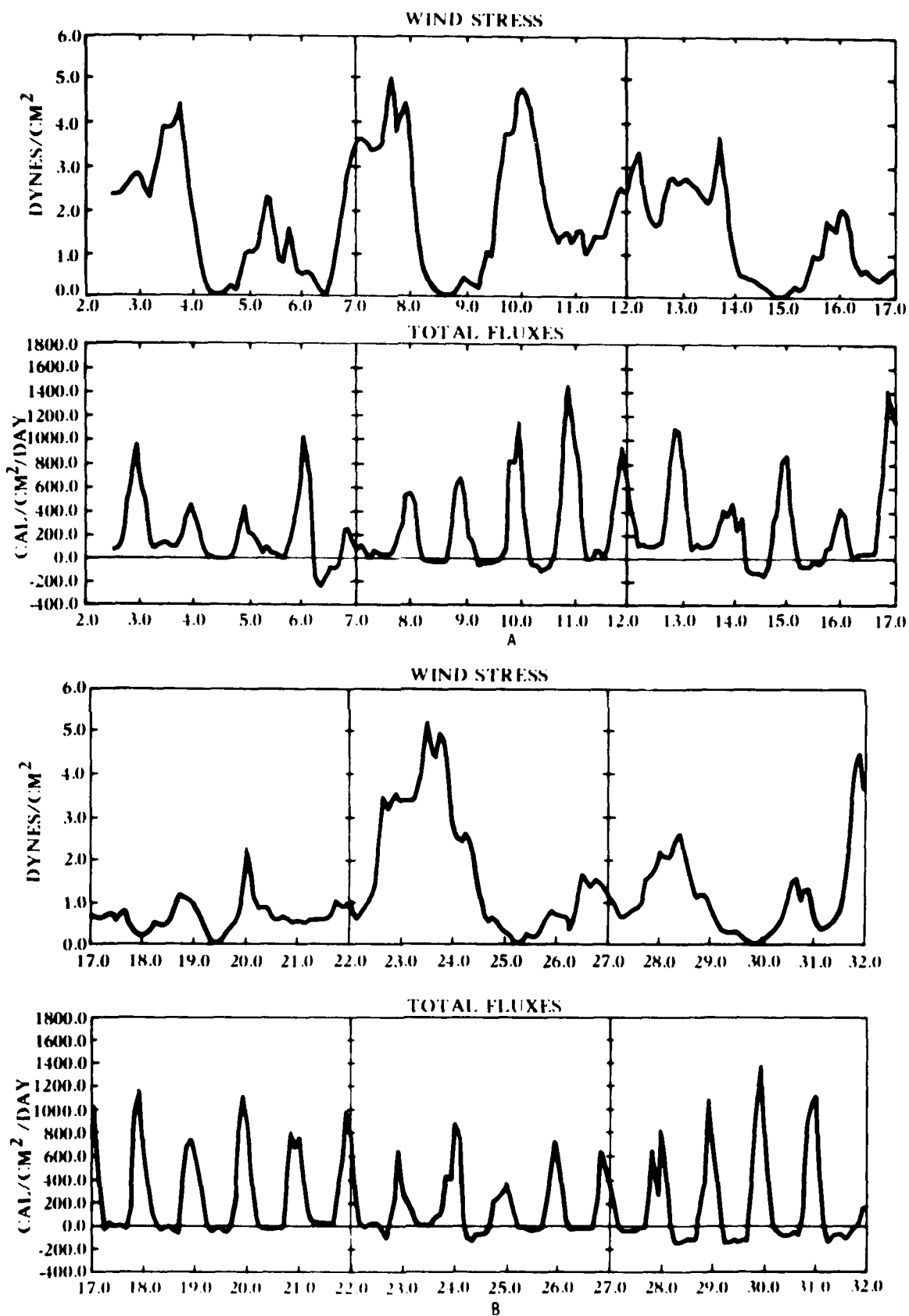


Figure 1. The atmospheric forcing fluxes of MILE.

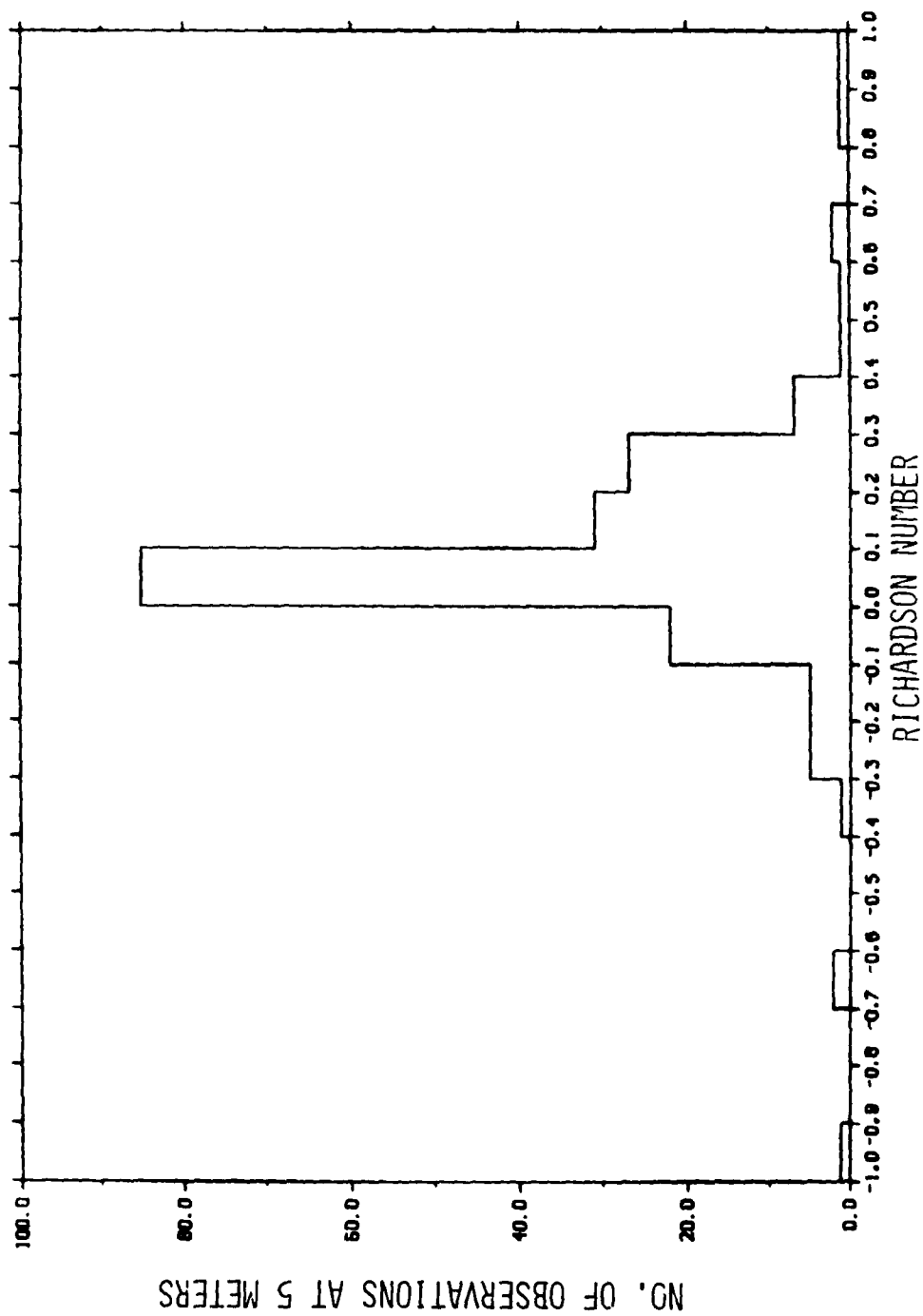


Figure 2. Distribution of flux Richardson numbers at 5 meters.

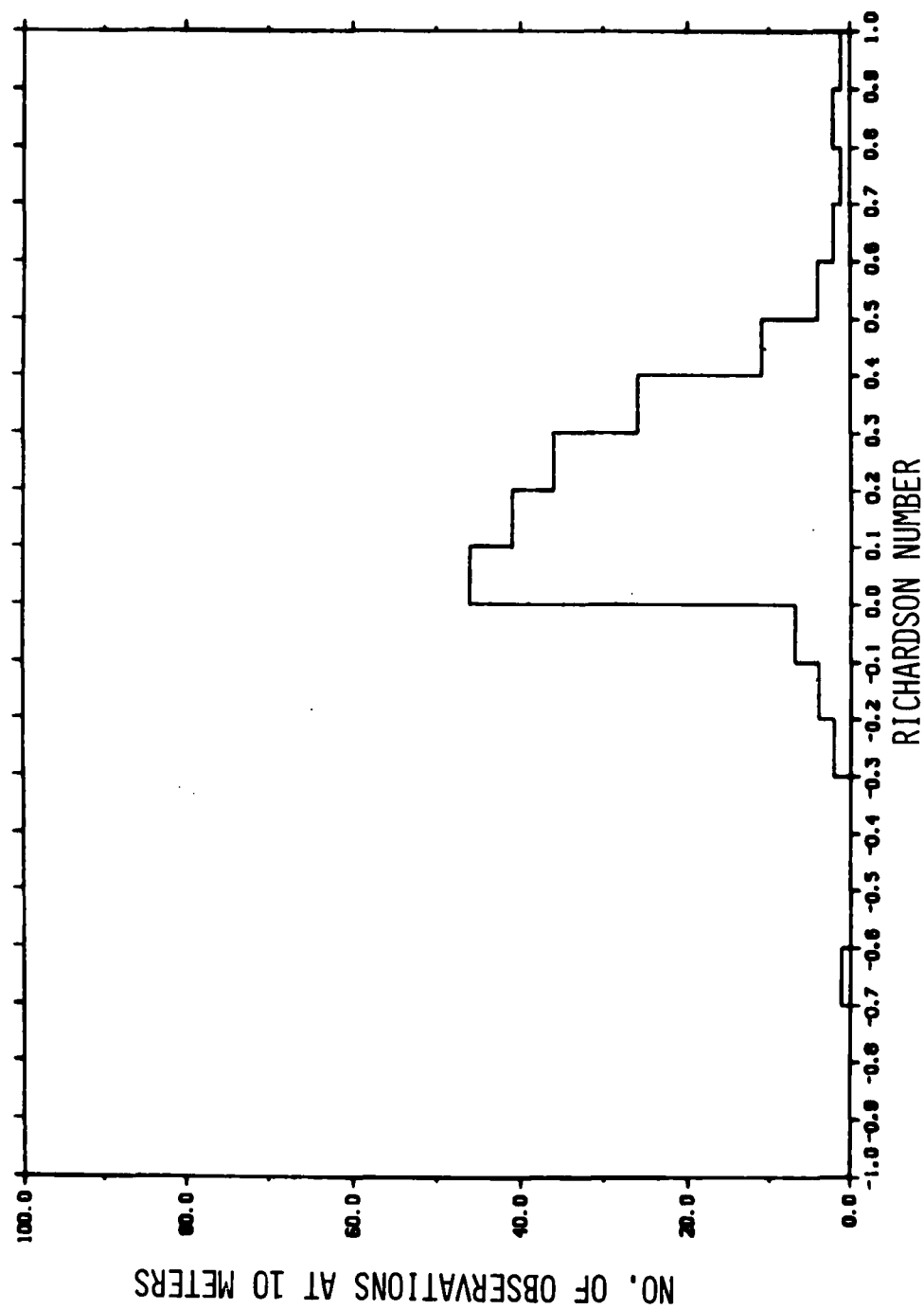


Figure 3. Distribution of flux Richardson numbers at 10 meters.

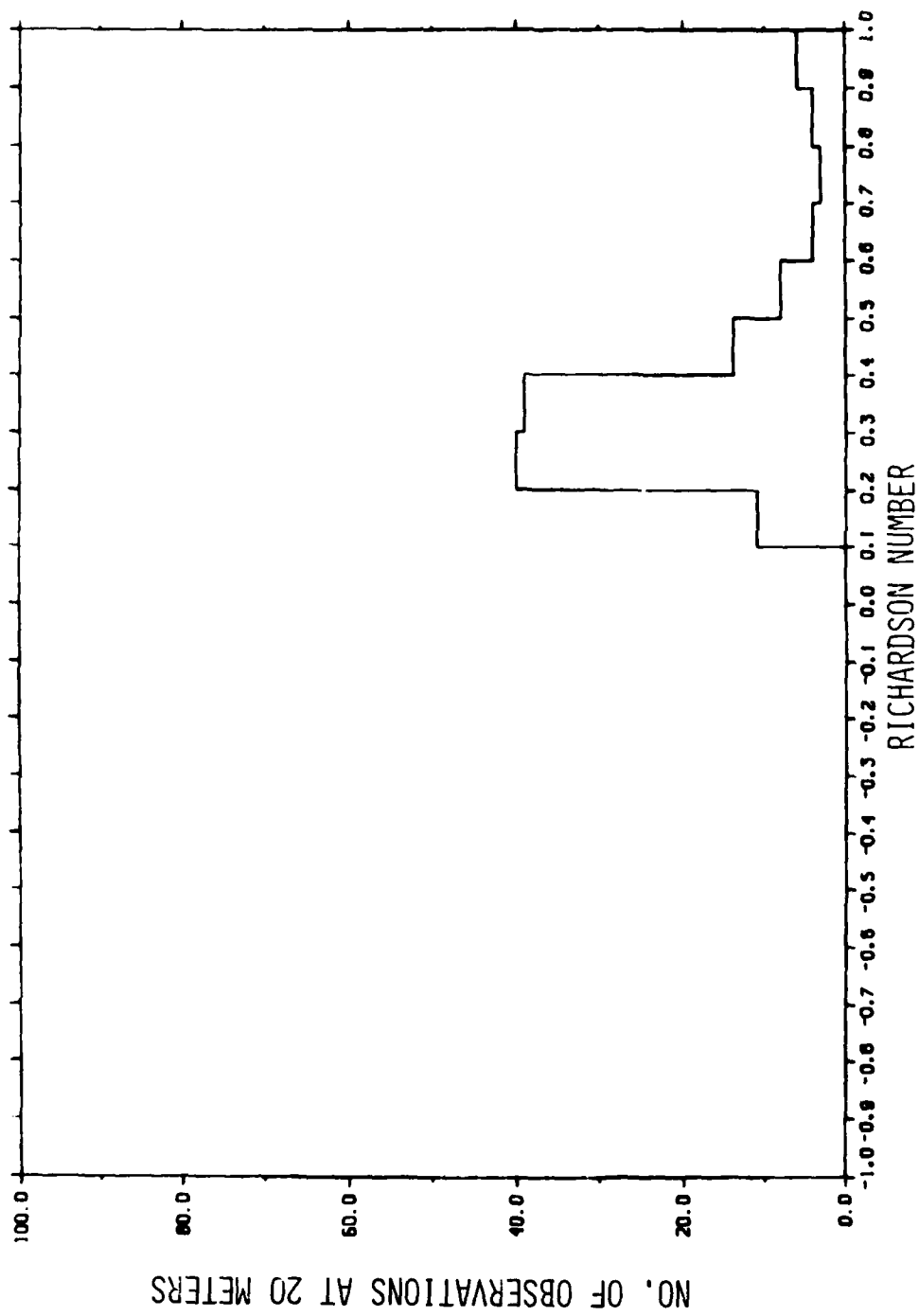


Figure 4. Distribution of flux Richardson numbers at 20 meters.

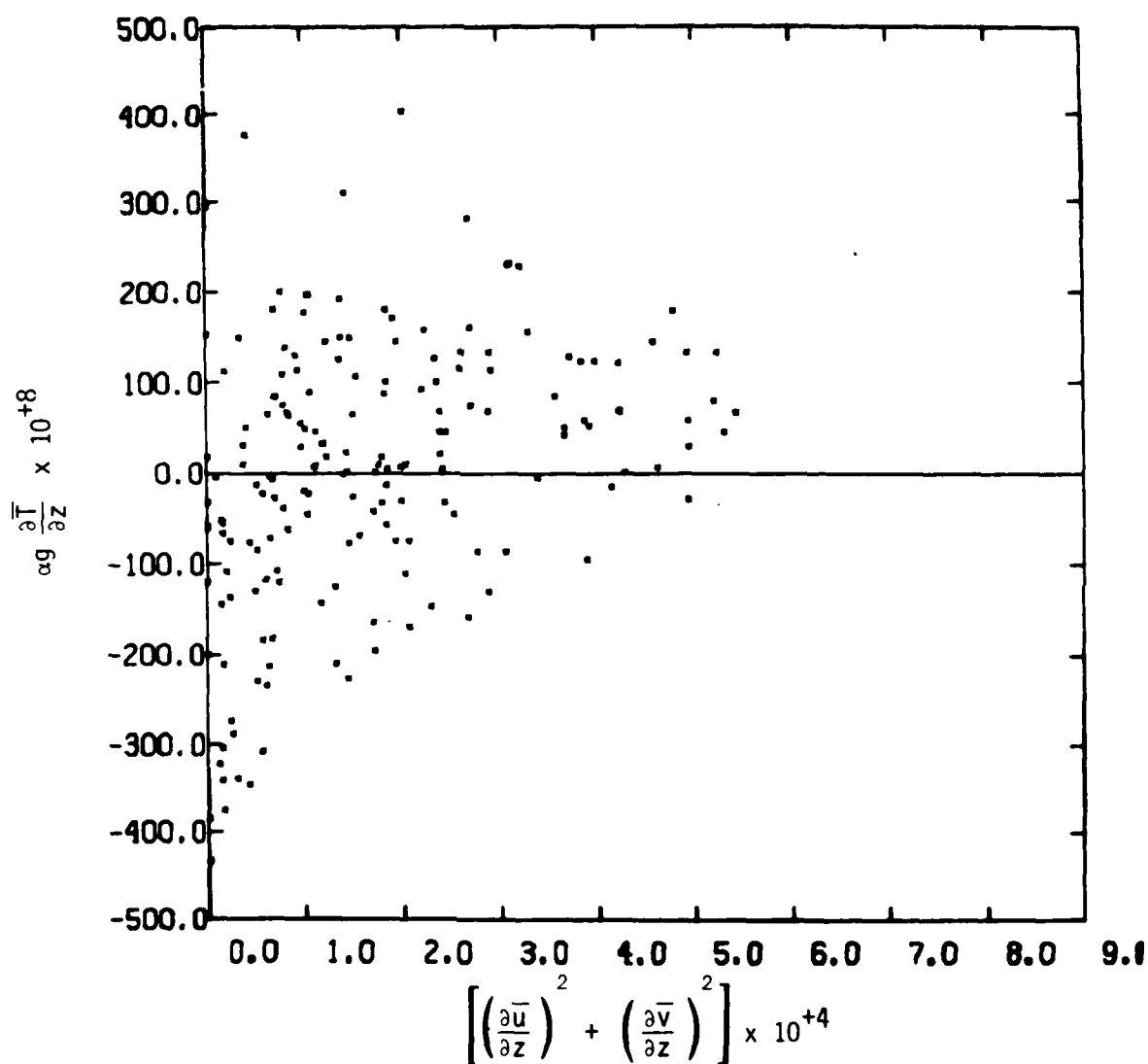


Figure 5. Scatter diagram of shear versus stratification at 1-meter depth.

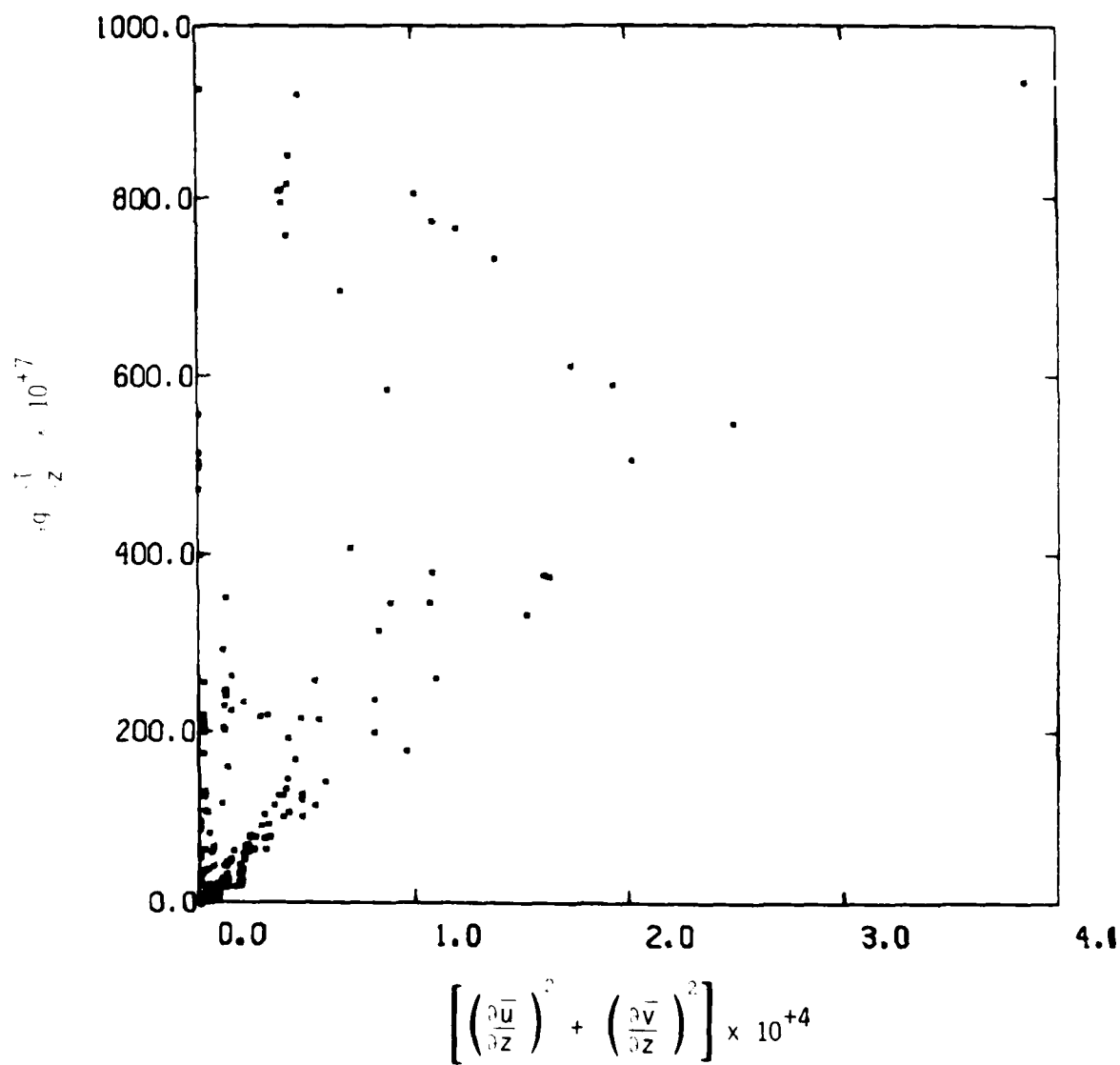


Figure 6. Scatter diagram of shear versus stratification at 20-meter depth.

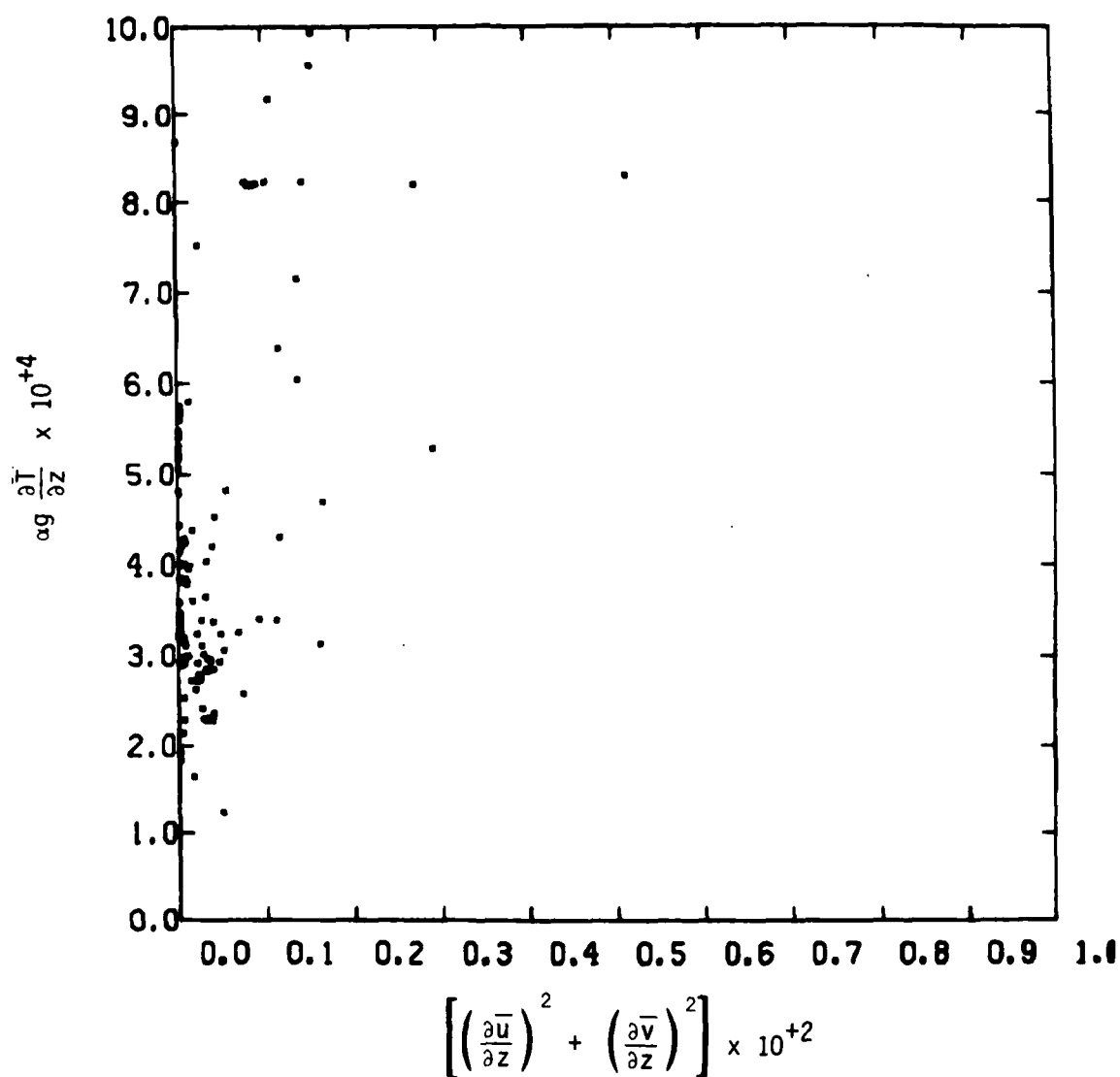


Figure 7. Scatter diagram of shear versus stratification at 30-meter depth.

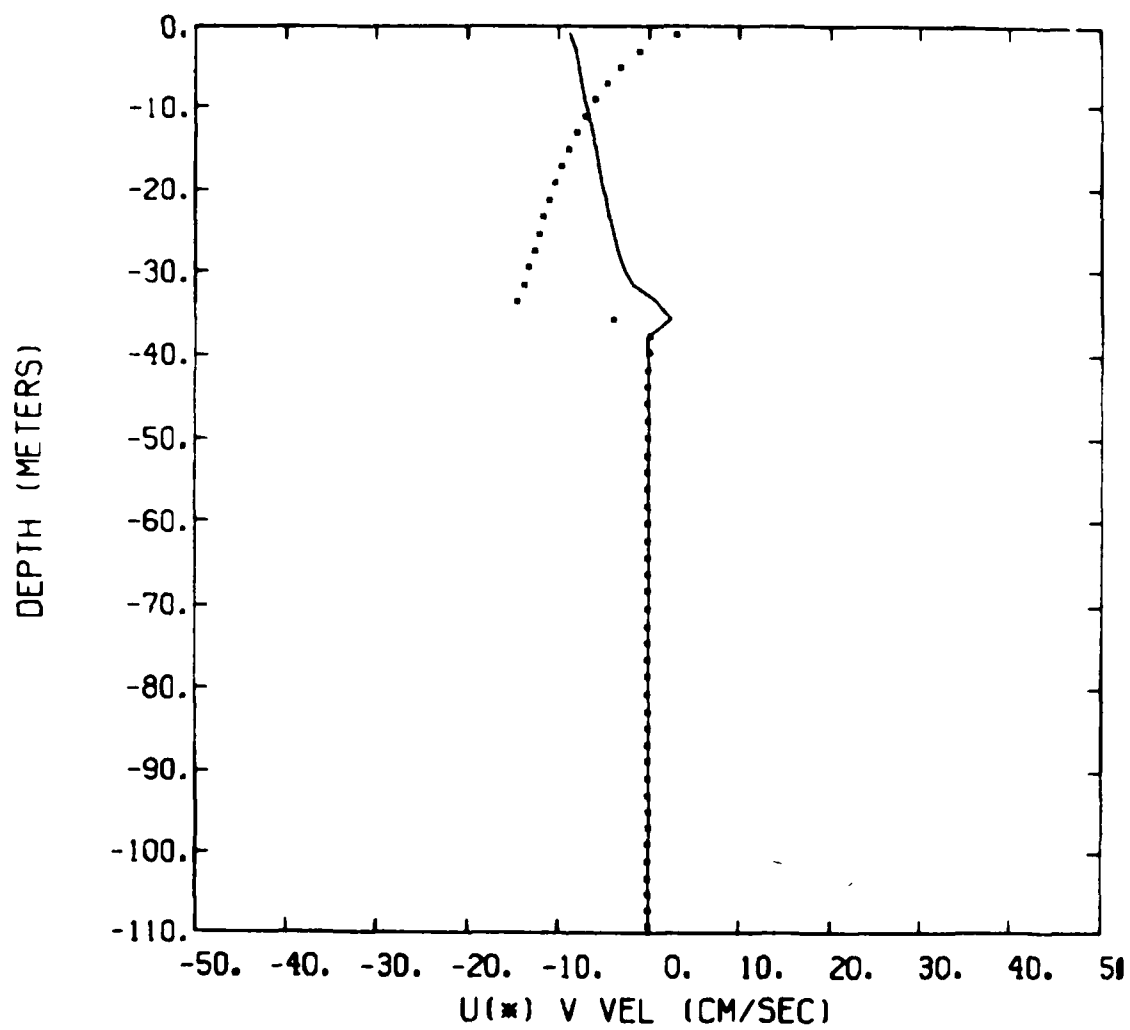


Figure 8. Total horizontal velocities versus depth.

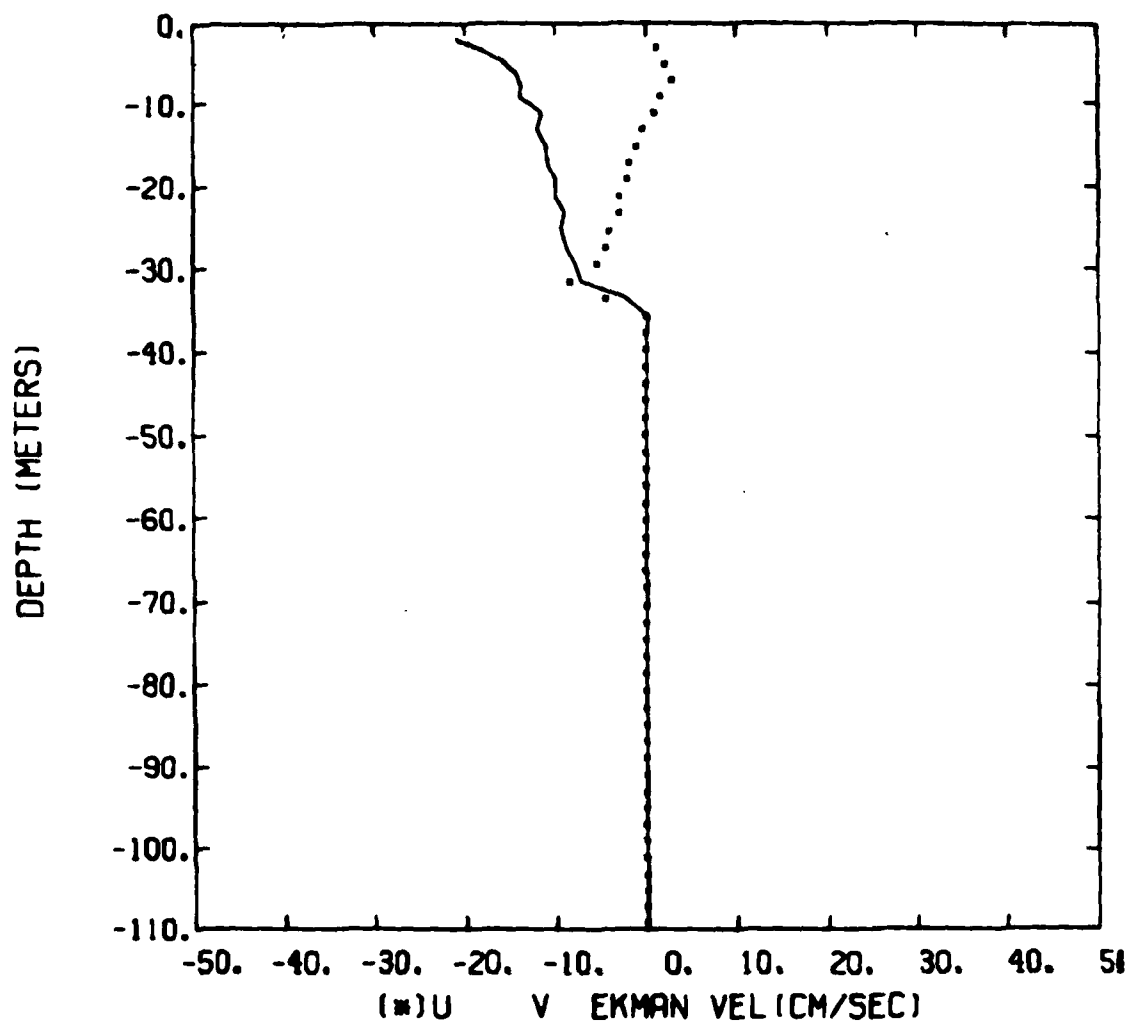


Figure 9. Ekman velocities versus depth.

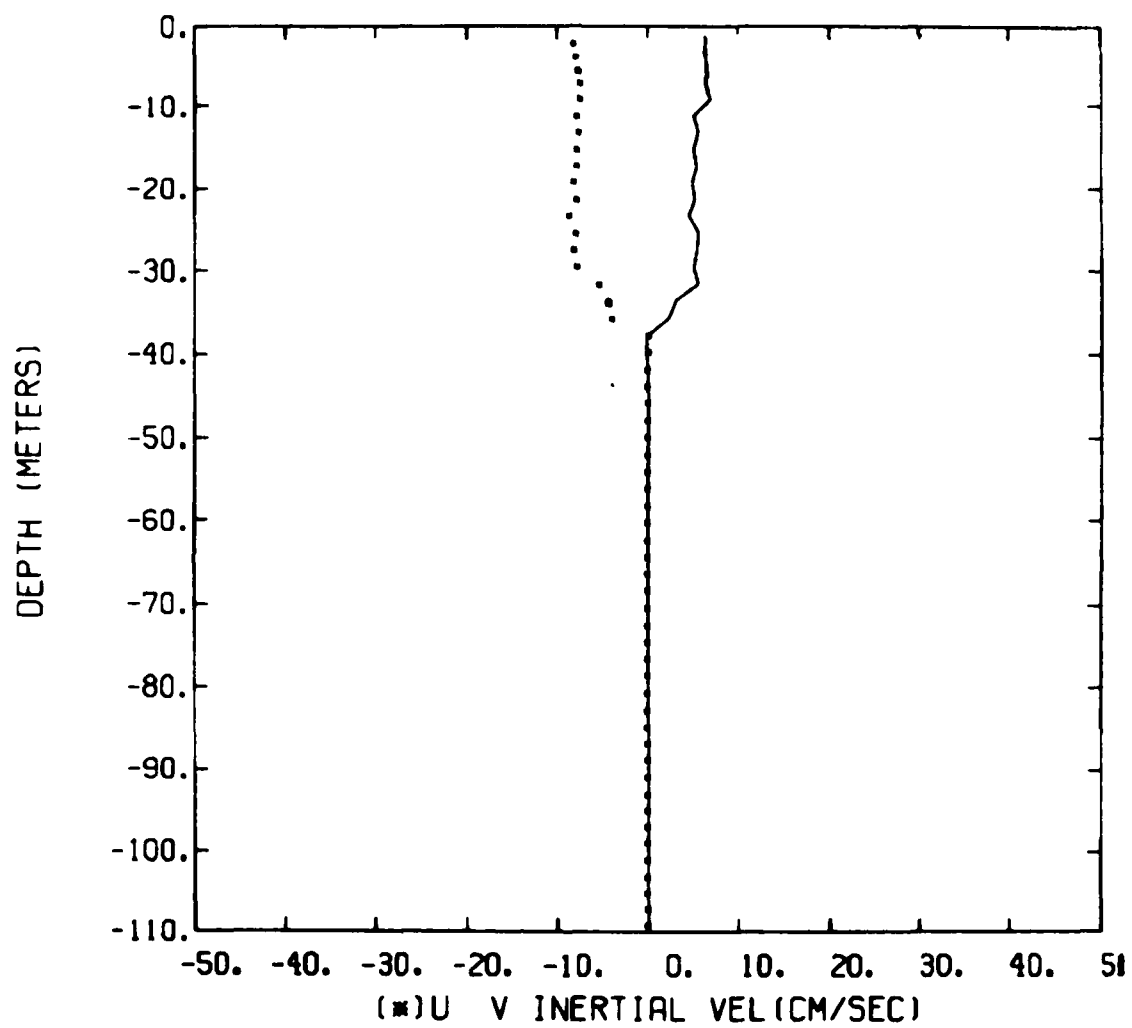


Figure 10. Inertial velocities versus depth.

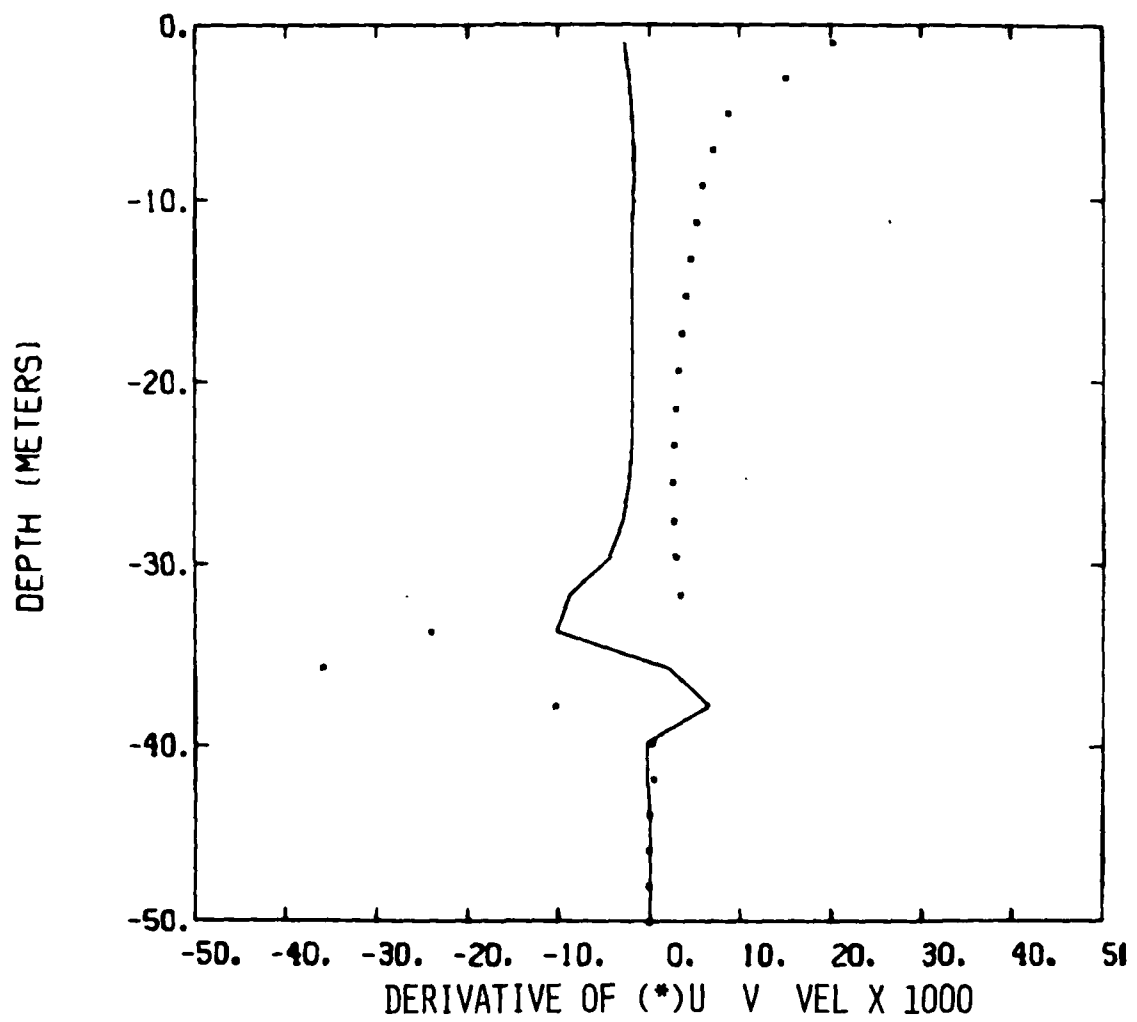


Figure 11. Derivatives of total horizontal velocities versus depth.

HODOGRAPH AT 1 METER

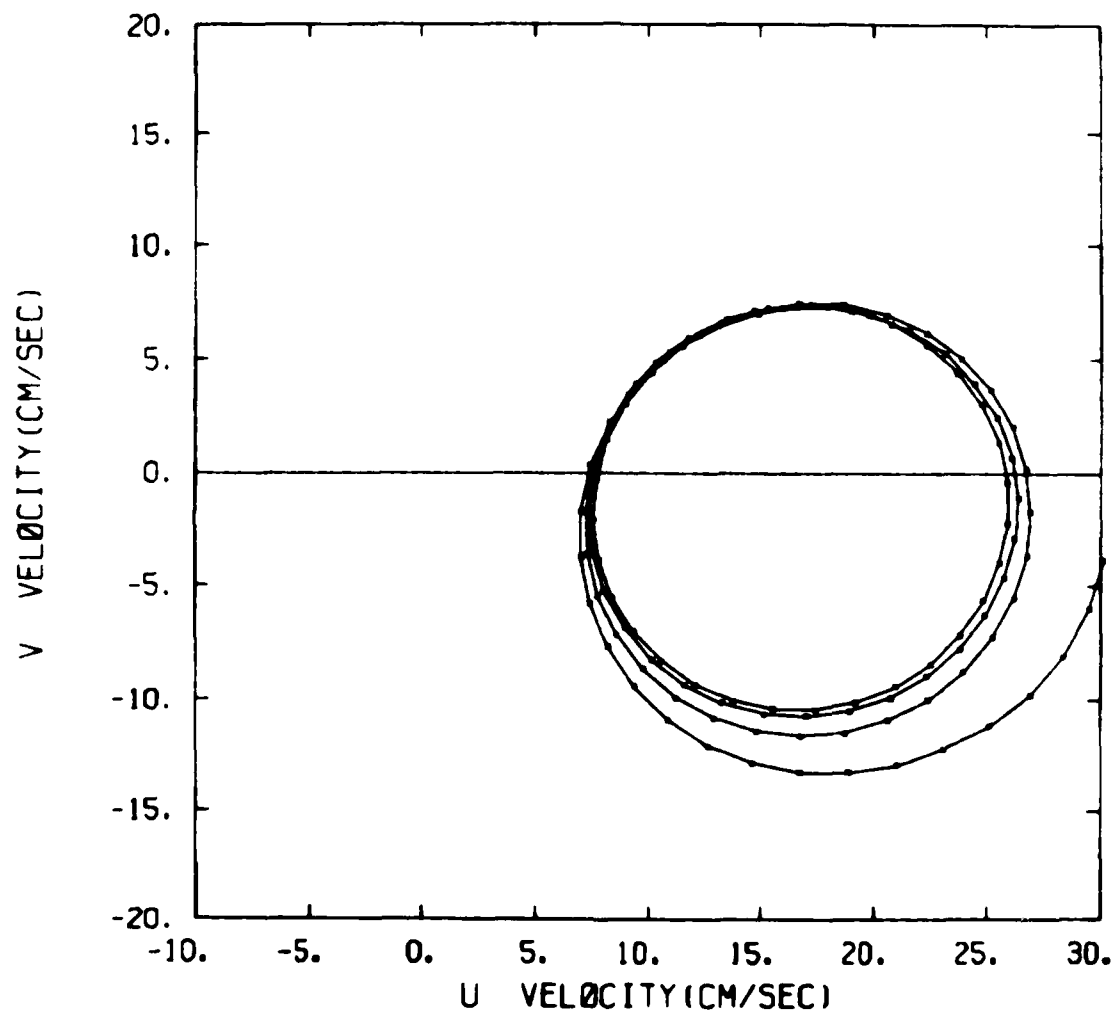


Figure 12. Velocity hodographs at 1-meter depth.

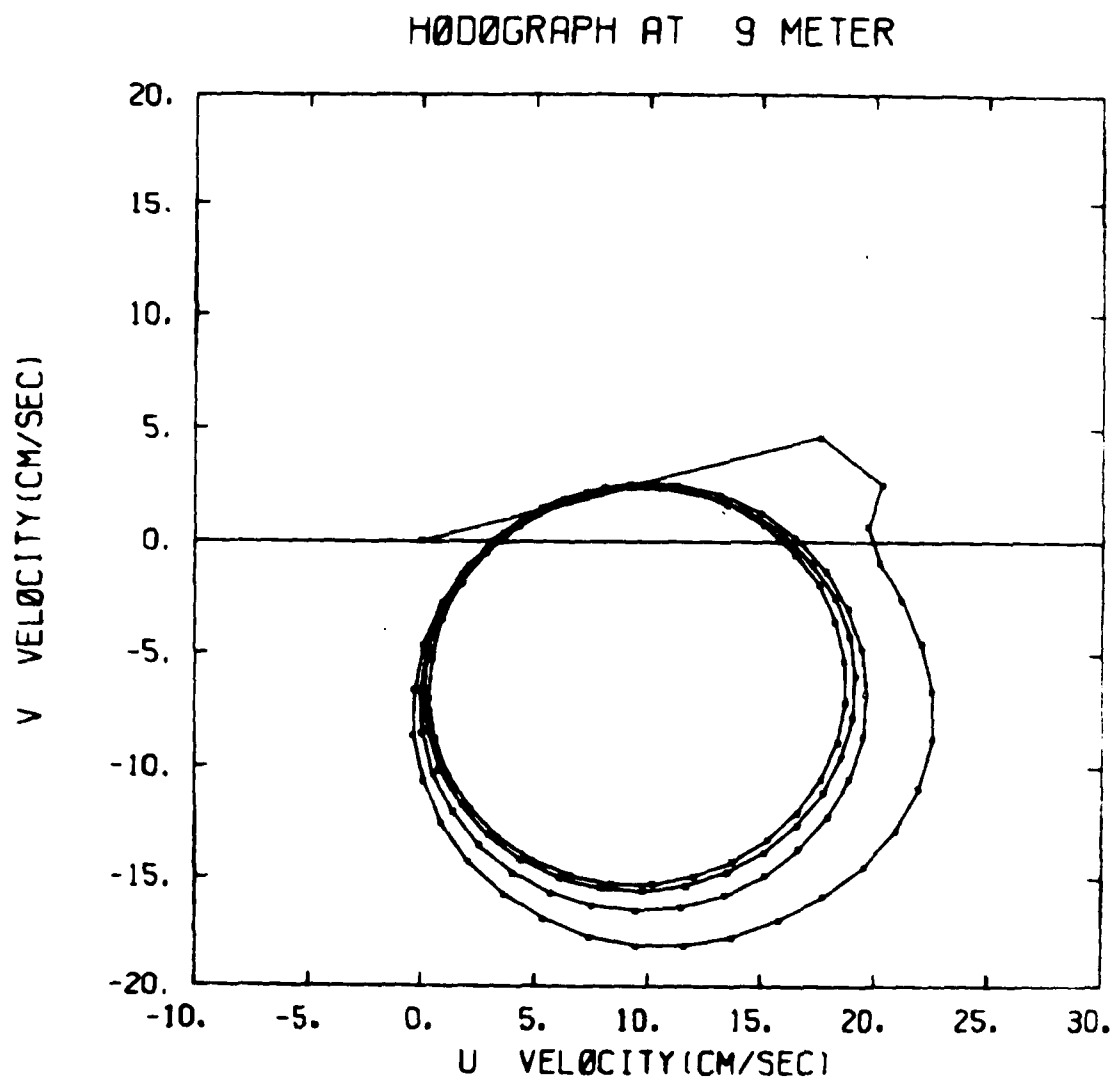


Figure 13. Velocity hodographs at 9-meter depth.

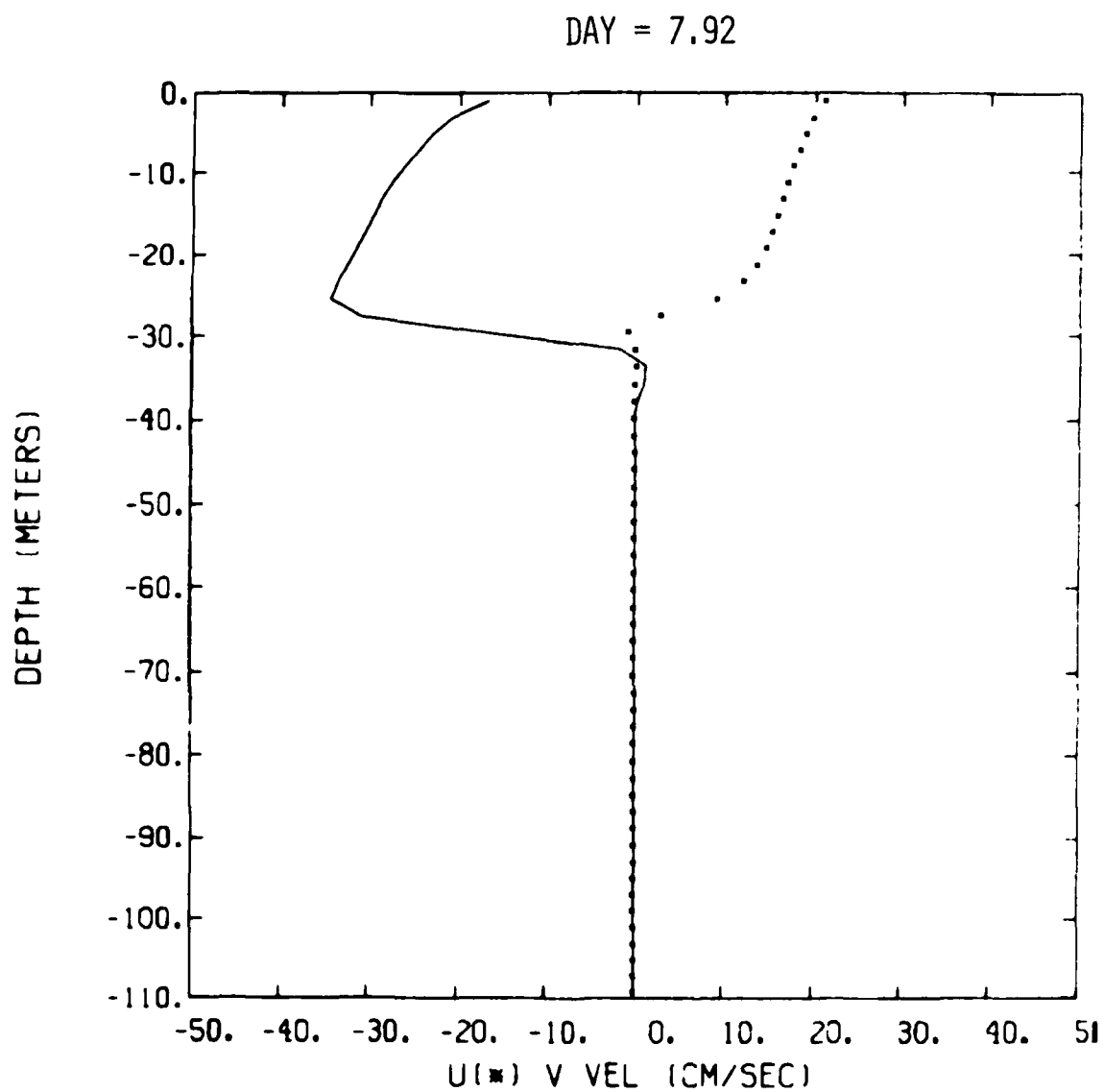


Figure 14. Total velocities versus depth on day 7.92.

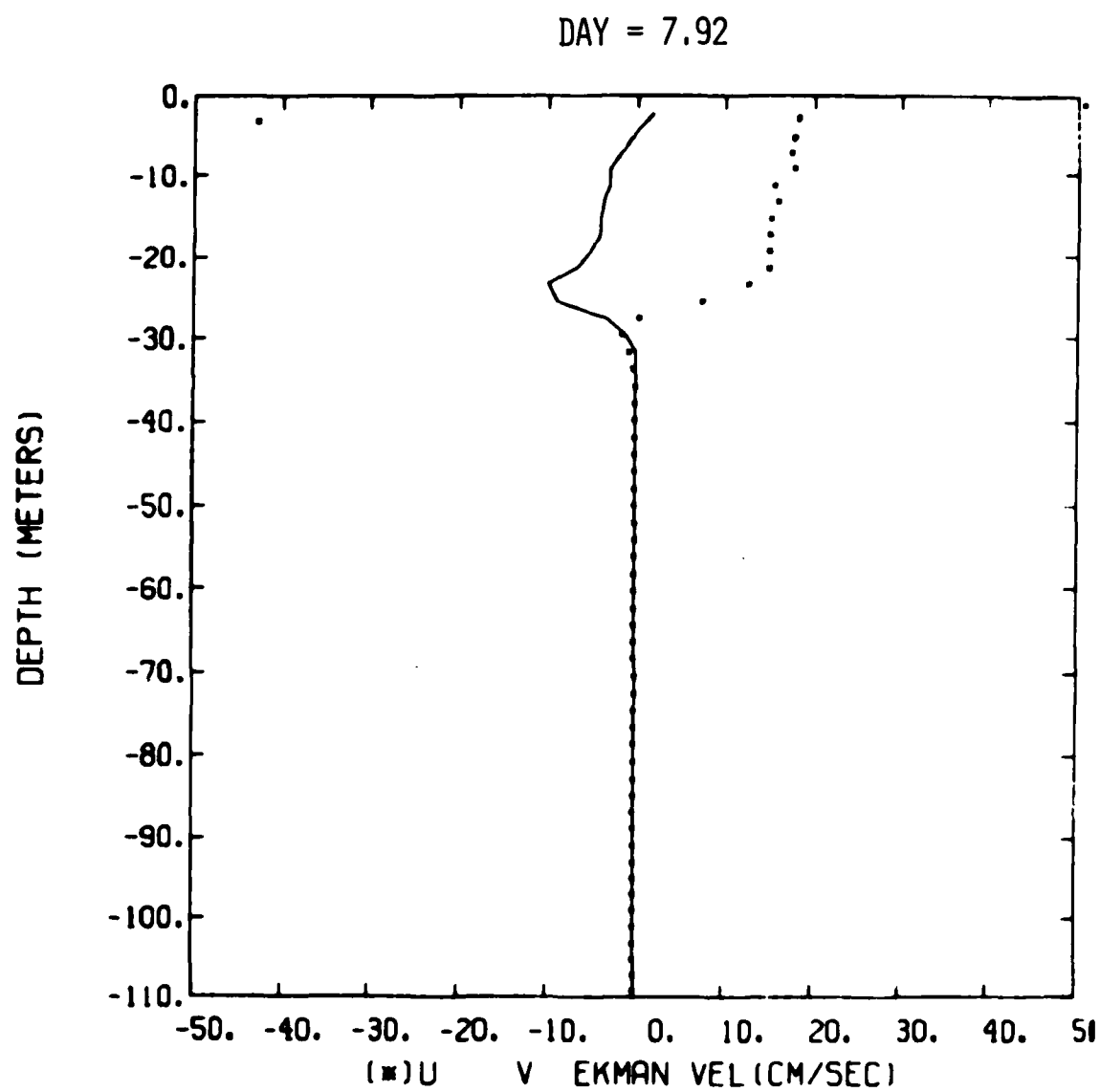


Figure 15. Ekman velocities versus depth on day 7.92.

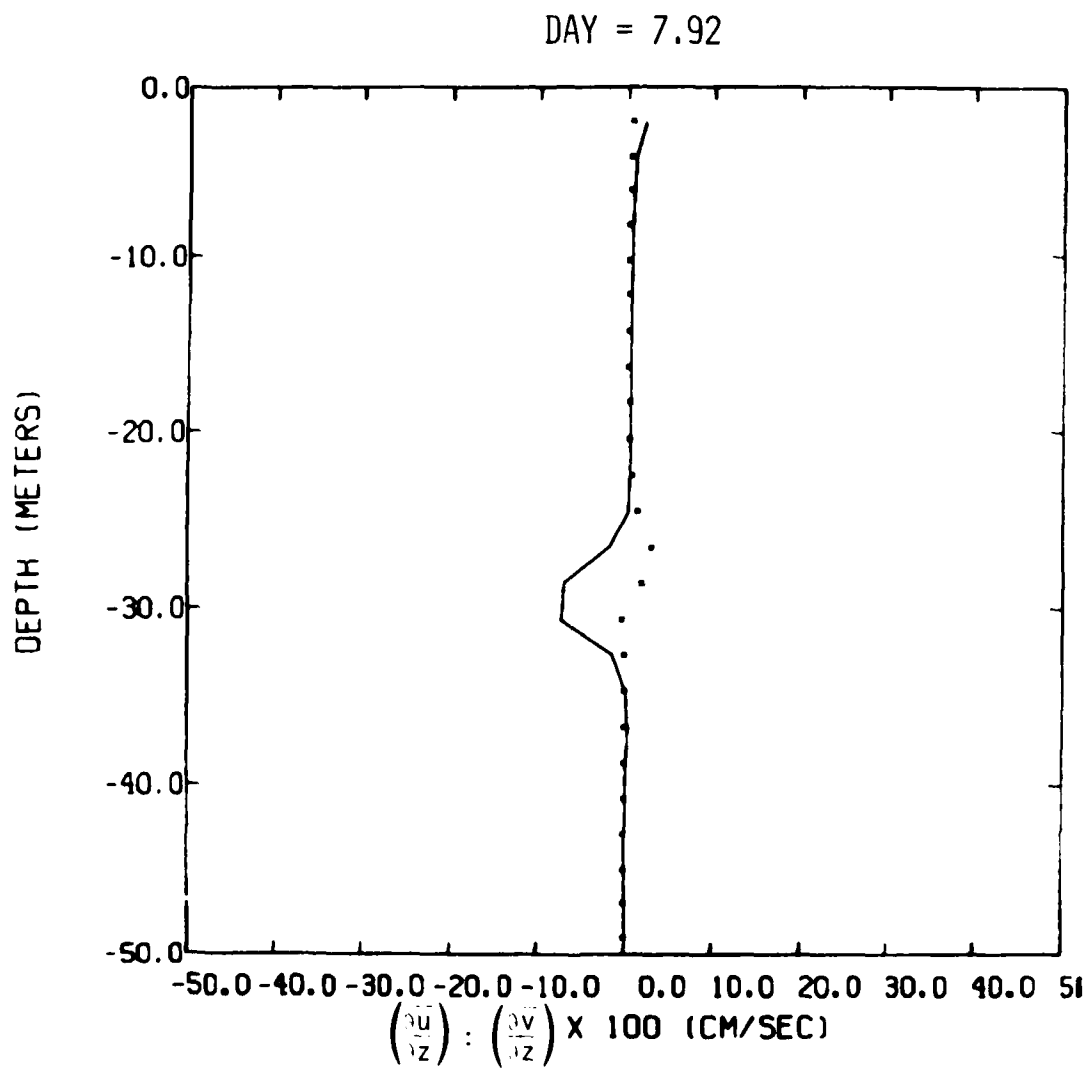


Figure 16. Shear versus depth on day 7.92.

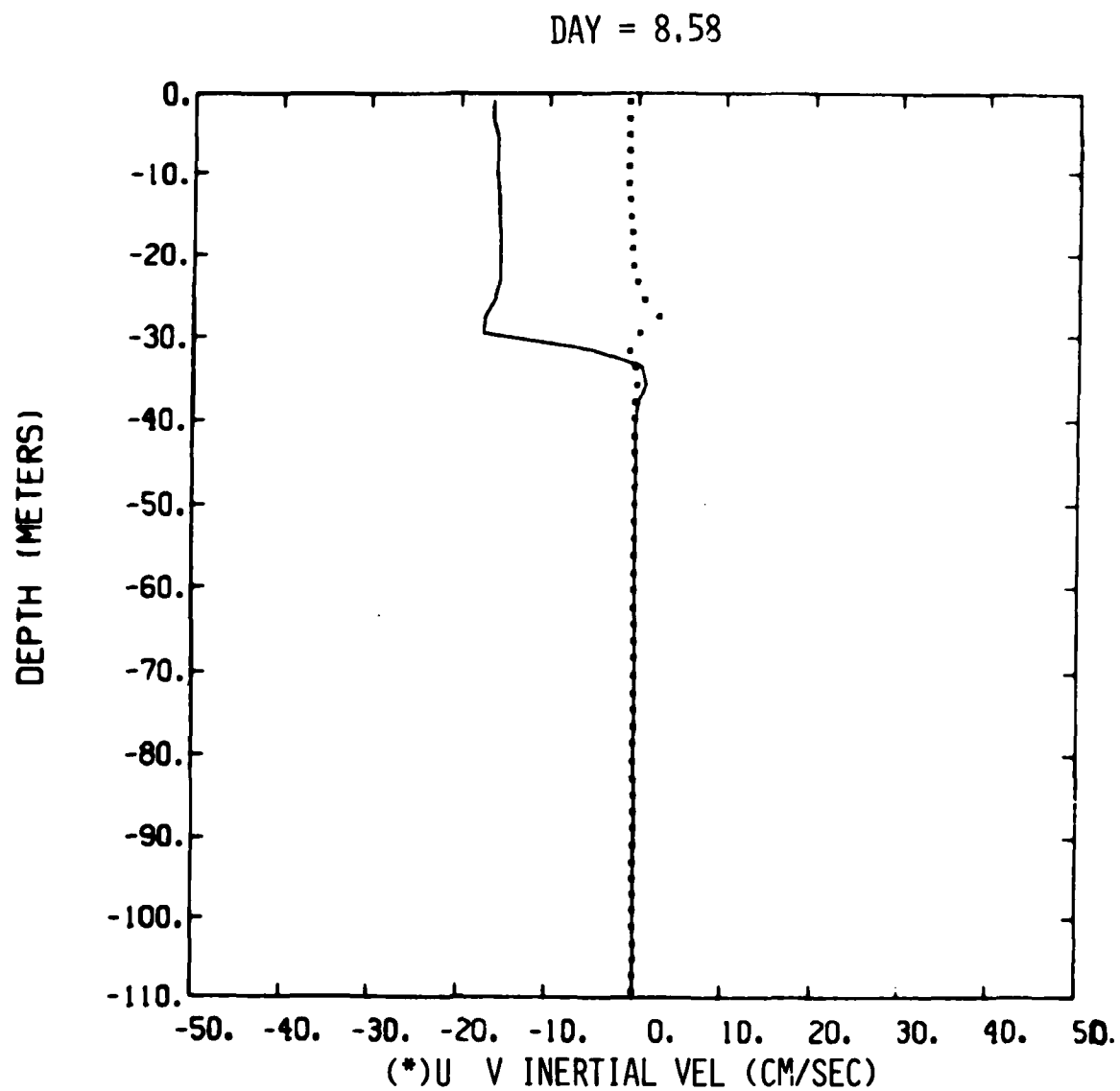


Figure 17. Inertial velocities versus depth on day 8.58.

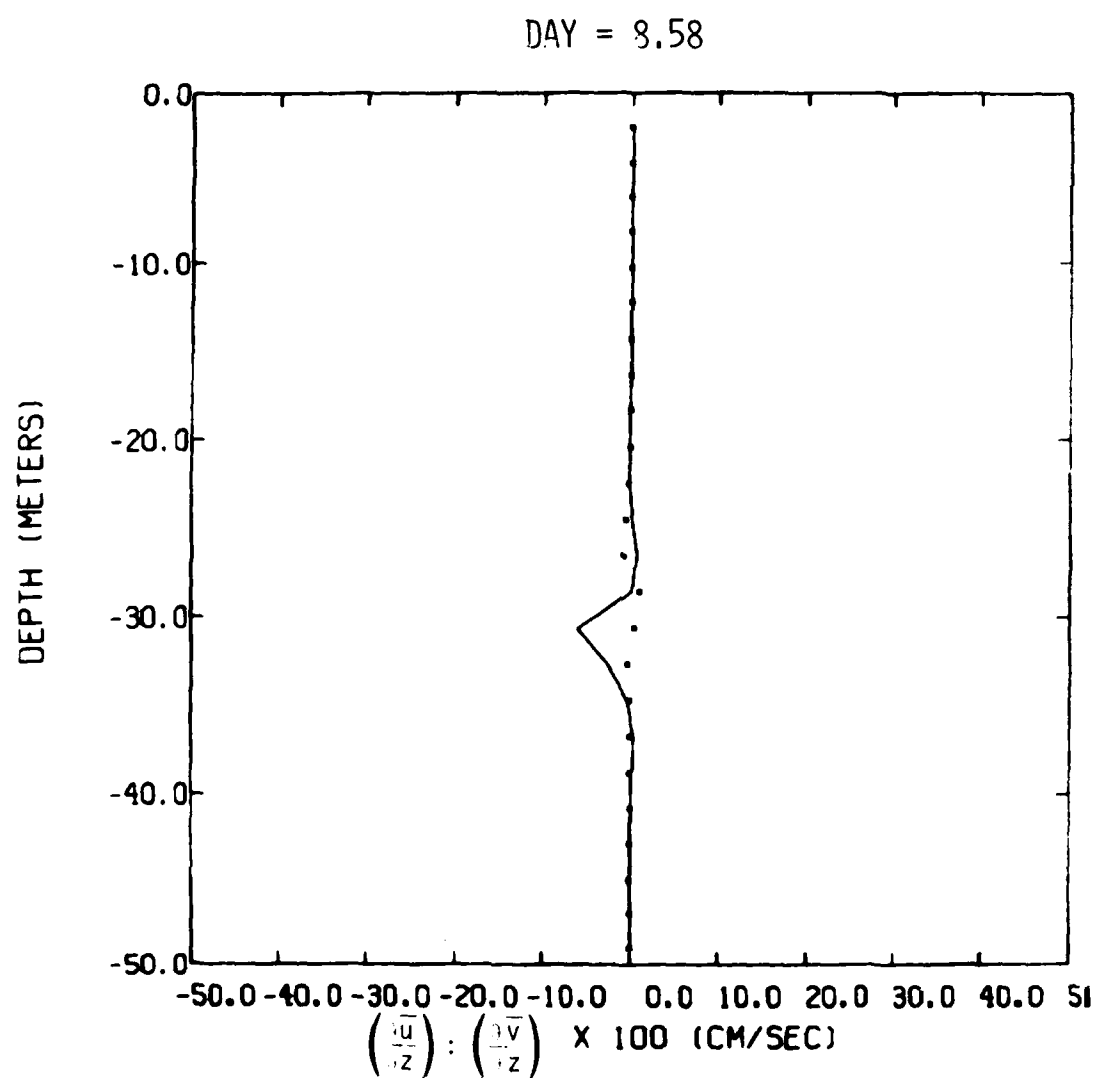


Figure 18. Shear versus depth on day 8.58.

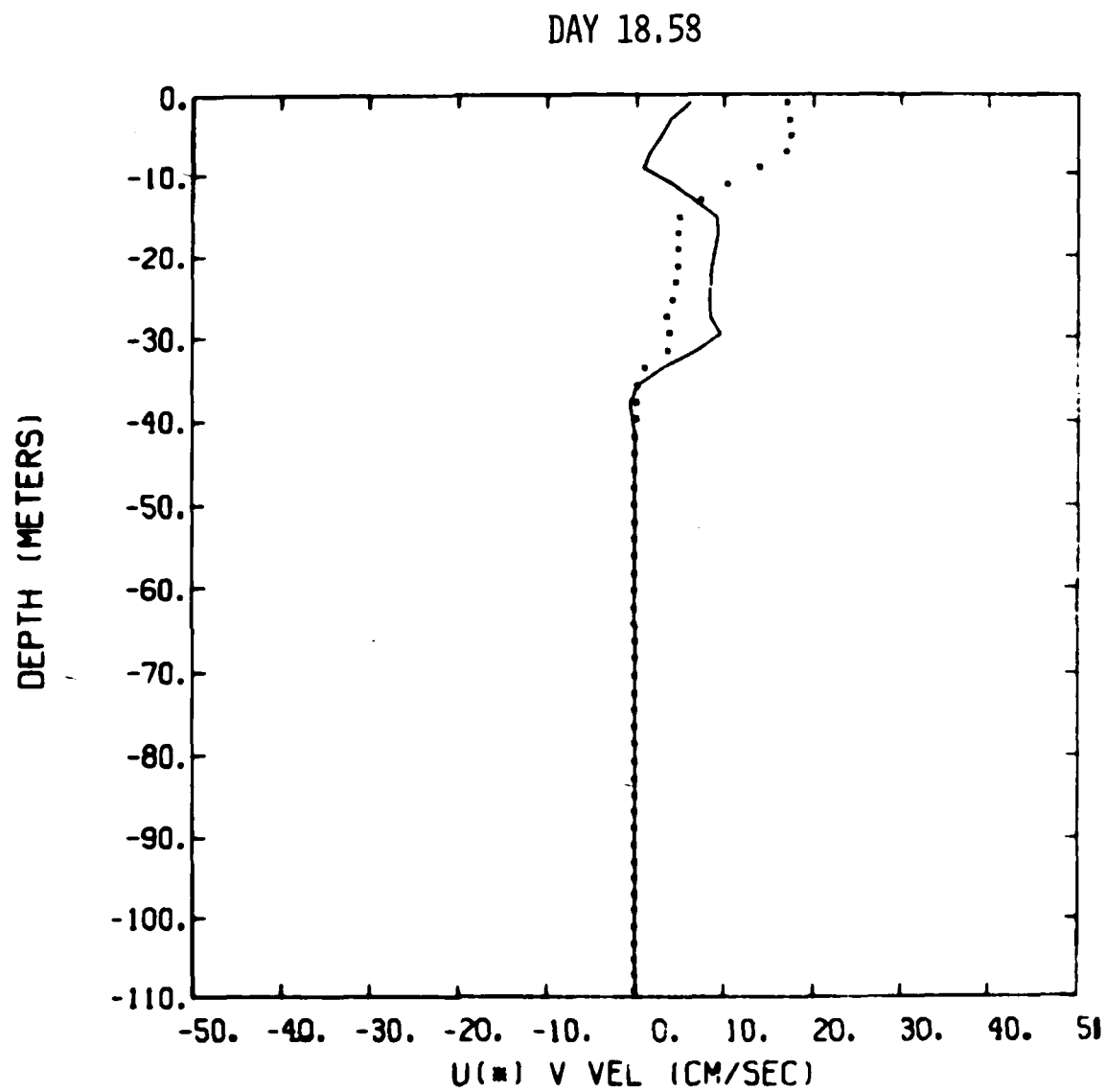


Figure 19. Total velocities versus depth on day 18.58.

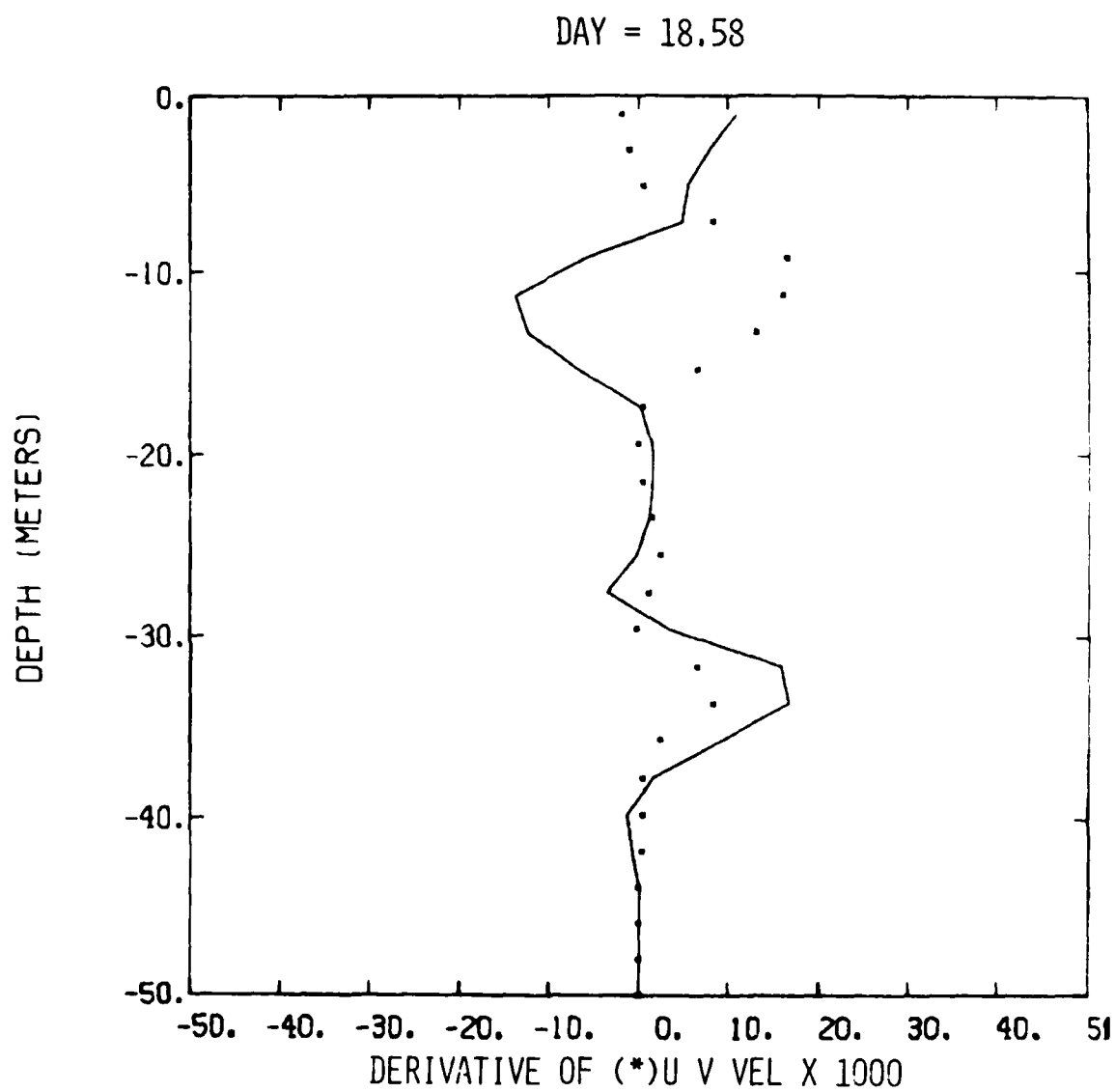


Figure 20. Shear versus depth on day 18.58.

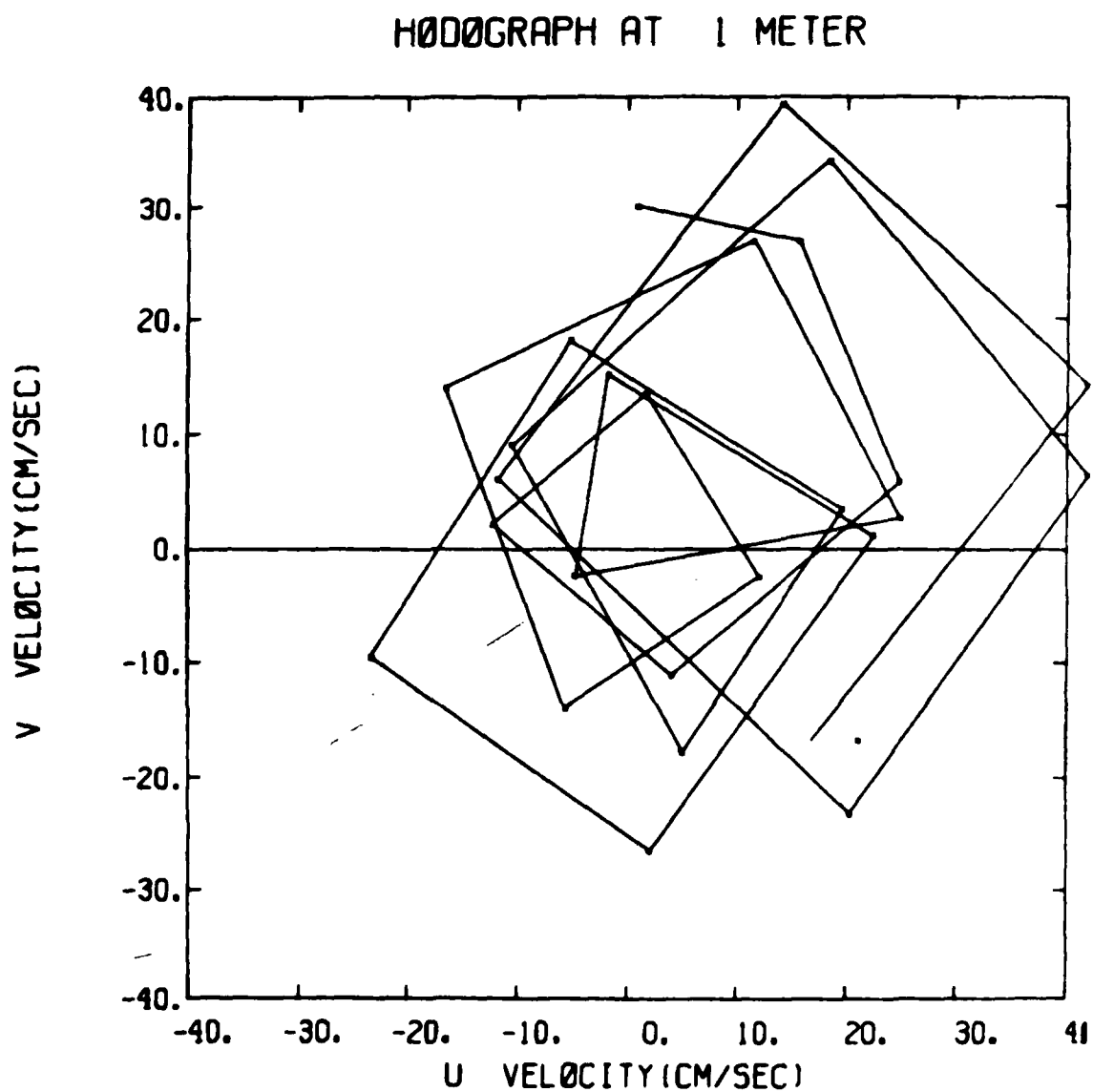


Figure 21. Velocity hodographs for MILE from day 2 to 7 at a depth of 1 meter.

HODOGRAPH AT 30 METER

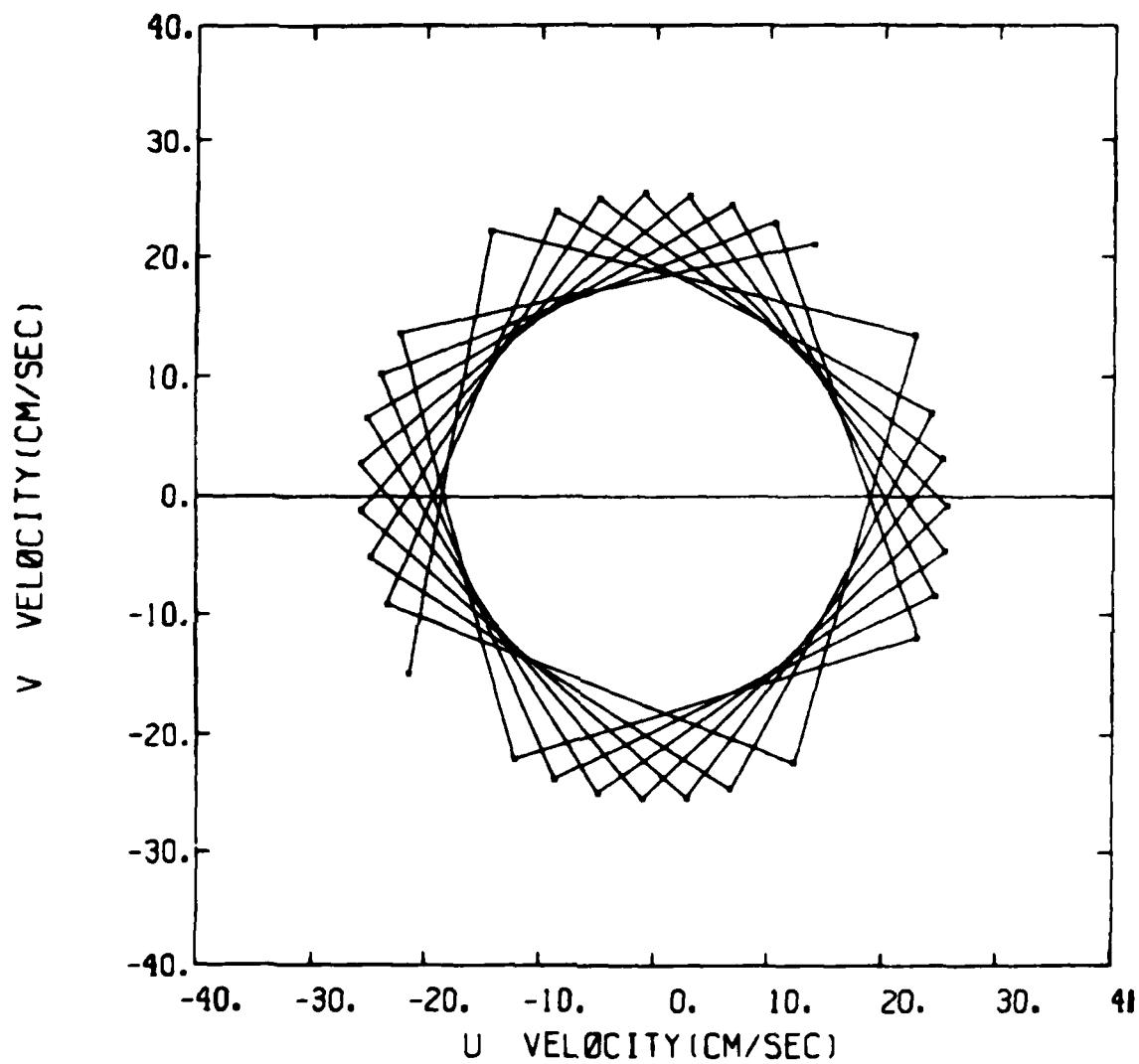


Figure 22. Velocity hodographs for MILE from day 32 to 36 at a depth of 30 meters.

APPENDIX THE FINITE-DIFFERENCE SCHEMES

For the WP model, the finite-difference equations are solved implicitly for \bar{u}^{n+1} , \bar{v}^{n+1} , \bar{T}^{n+1} . This involves, as explained in the WP paper, solving algebraically the finite-difference equations for the second-order correlations. The resultant finite-difference equations for the mean fields are, then, in the desirable diffusive-type form plus a forcing term. The diffusive form is desirable because it enables one to solve implicitly for the mean fields. As an illustration, the resultant equation for temperature is as follows:

$$\frac{\bar{T}^{n+1} - \bar{T}^{n-1}}{2\Delta t} = \frac{\partial}{\partial z} \left(K_T \frac{\partial \bar{T}^{n+1}}{\partial z} \right) - \frac{\partial}{\partial z} \left\{ \frac{\alpha g R_{TT}}{\frac{1}{2\Delta t} + C_1 \left(\frac{\epsilon}{k} \right)} + R_{WT} \right\} /$$

$$\left[\frac{1}{2\Delta t} + C_1 \left(\frac{\epsilon}{k} \right) + \frac{3\alpha g (\partial \bar{T} / \partial z)}{(1/2\Delta t) + C_1 \left(\frac{\epsilon}{k} \right)} \right] + \frac{1}{\rho_0 c_p} \frac{\partial \bar{F}}{\partial z}, \quad (1)$$

where

$$K_T = \frac{\left[C_3 \epsilon + (\overline{w'w'})^{n-1} / 2\Delta t \right] - \frac{\partial}{\partial z} \overline{w'w'w'}^n}{\left[\frac{1}{2\Delta t} + C_1 \left(\frac{\epsilon}{k} \right) \right] \left[\frac{1}{2\Delta T} + C_1 \left(\frac{\epsilon}{k} \right) + \frac{3\alpha g (\partial \bar{T} / \partial z)}{(1/2\Delta t) + C_1 \left(\frac{\epsilon}{k} \right)} \right]}$$

$$R_{TT} = \frac{\overline{TT}^{n-1}}{2\Delta t} - \frac{\partial}{\partial z} (\overline{T'T'w'})^n, \quad \text{and} \quad R_{WT} = \frac{\overline{w'TT}^{n-1}}{2\Delta t} - \frac{\partial}{\partial z} (\overline{w'w'TT})^n.$$

The treatment of the Coriolis terms are changed from the one stated in the WP paper. The method of time splitting is now used to separate them from the rest of the solution. This treatment is illustrated in equation (2.1). The finite-difference analogy is

$$\frac{\bar{u}^* - \bar{u}^{n-1}}{2\Delta t} = \frac{\partial}{\partial z} \left(K_u \frac{\partial \bar{u}^*}{\partial z} \right) + S_u + \nabla \frac{\partial^2 \bar{u}^*}{\partial z^2} \quad (2)$$

$$\frac{\bar{u}^{n+1} - \bar{u}^*}{2\Delta t} = +f\bar{v}^n \quad (3)$$

where K_u is the eddy coefficient term, s_u is the source term, and \bar{u}^* is the intermediate time value. This method was introduced so as not to overdamp the inertial oscillations.

The grid is stretched. The stretching of the grid and the resultant accuracy of the overall finite-difference scheme is described in the WP paper.

DISTRIBUTION

<u>Number of Copies</u>	<u>To</u>
1	NORDA Code 100
1	320
1	322
1	300
1	330
1	331
1	335
4	540
1	Commanding Officer
1	Liaison Office
1	CNR
1	ONR Code 103T (Dr. S. G. Reid)
1	COMNAVOCEANO
1	NAVOCEANO Code 7004
1	NAVOCEANO Code 7200
1	OP-95T (Dr. A. Andreassen)
1	OP-952 (CDR J. Harlett)
1	ONR (Dr. R. Winokur)
1	OP-212E
4	APL/JHU (Dr. G. D. Smith, Dr. L. J. Crawford, Dr. G. G. Meritt, Dr. H. E. Gilreath)
1	APL/UW (Dr. T. B. Sanford)
1	ASN (RE&S)
1	SSPO (Dr. P. A. Selwyn)
1	NAVELEX 320
1	NAVELEX PME-124
1	NCSL - Panama City
1	PM-2 (Mr. Bill Welsh)
1	NSRDC (Mr. W. J. Andahazy) Code 2704
1	University of Washington Applied Physics Laboratory Attn: Dr. Michael C. Gregg 1013 Northeast 40th Street Seattle, WA 98105
1	University of Washington Applied Physics Laboratory Attn: Dr. Thomas B. Sanford 1013 Northeast 40th Street Seattle, WA 98105

DISTRIBUTION

Number of Copies

To

1	Marine Physical Laboratory Scripps Institution of Oceanography Attn: Dr. Rob Pinkel University of California, San Diego La Jolla, CA 92037
2	Science Applications, Inc. Attn: Dr. Richard Lambert, Jr., and Dr. W. Grabowski 8400 Westpark Drive McLean, VA 22101
1	Science Applications, Inc. Attn: Dr. A. D. Kirwan 4348 Carter Creek Parkway, Suite 101 Bryan, TX 77801
1	University of British Columbia Attn: Dr. Thomas R. Osborn Vancouver, BC Canada V6T 1W5
1	Commanding Officer Naval Research Laboratory Attn: Dr. John Dugan Department of the Navy Washington, DC 20375

UNCLASSIFIED

SECURITY CLASSIFICATION OF THIS PAGE (When Data Entered)

9 REPORT DOCUMENTATION PAGE		READ INSTRUCTIONS BEFORE COMPLETING FORM
1. REPORT NUMBER NORDA Technical Note	2. GOVT ACCESSION NO. AD-A098902	3. RECIPIENT'S CATALOG NUMBER
4. TITLE (and Subtitle) An Analysis of Modelled Shear Distributions During the <u>MILE</u> Experiment.		5. TYPE OF REPORT & PERIOD COVERED
7. AUTHOR(s) Warn-Varnas son		6. PERFORMING ORG. REPORT NUMBER
9. PERFORMING ORGANIZATION NAME AND ADDRESS NORDA, Code 322, Bldg. 1100 NSTL Station, MS 39529		8. CONTRACT OR GRANT NUMBER(s) Various
11. CONTROLLING OFFICE NAME AND ADDRESS 141 W F D - 711		10. PROGRAM ELEMENT, PROJECT, TASK AREA & WORK UNIT NUMBERS 1021
14. MONITORING AGENCY NAME & ADDRESS (if different from Controlling Office)		12. REPORT DATE 2/1/81
		13. NUMBER OF PAGES
		15. SECURITY CLASS. (of this report) UNCLASSIFIED
		15a. DECLASSIFICATION/DOWNGRADING SCHEDULE
16. DISTRIBUTION STATEMENT (of this Report) UNLIMITED		
17. DISTRIBUTION STATEMENT (of the abstract entered in Block 20, if different from Report)		
18. SUPPLEMENTARY NOTES		
19. KEY WORDS (Continue on reverse side if necessary and identify by block number) Shear distributions, inertial velocity, Ekman velocity, velocity hodographs, one-dimensional mixed layer model, stratification		
20. ABSTRACT (Continue on reverse side if necessary and identify by block number) The shear in the mixed layer was forecasted and studied for the duration of the MILE experiment. The forecasting was done with the Warn-Varnas and Piacsek (1979) model. The forecasts were initiated from data and driven by the experimentally - measured wind stress, radiation, and latent and sensible heat flux. The duration of forecasts spanned a time frame of several days to a month. The problem of understanding the shear in the mixed-layer region during MILE was approached from two points of view. First, the basic dynamic processes		

DD FORM 1 JAN 73 1473

EDITION OF 1 NOV 65 IS OBSOLETE

UNCLASSIFIED

SECURITY CLASSIFICATION OF THIS PAGE (When Data Entered)

UNCLASSIFIED

SECURITY CLASSIFICATION OF THIS PAGE(When Data Entered)

that generate shear were considered. Second, statistical distributions of shear as a function of depth and time were computed.

The basic dynamics can be understood by decomposing the velocity into an Ekman-type component and an inertial component. The vertical structure of the velocity can be visualized as a superposition of an inertial oscillation onto an Ekman spiral; the inertial oscillations being excited by abrupt changes in wind stress. In most cases, the maximum shear occurred at the bottom of the mixed layer and near the surface. In some cases, two shear maxima regions were found below the surface. These cases involved situations of rising wind stress from a previous history of low magnitude.

In the statistical approach, scatter diagrams of shear versus Brunt-Vaisala frequency are computed. At different depths, these scatter diagrams show the relationship of mixing, as indicated by the Brunt-Vaisala frequency, to shear. The simulated magnitudes of shear are in the range of the experimental results of R. E. Davis, et al.

Probability diagrams of calculated Richardson numbers as a function of depth are also computed. These probability diagrams show a shift toward higher Richardson numbers as the depth increases. This reflects the fact that the penetration of turbulence and mixing tend to decrease, on the average, with depth.

UNCLASSIFIED

SECURITY CLASSIFICATION OF THIS PAGE(When Data Entered)

END

DATE
FILMED

6-81

DTIC